

Article

Structural Properties and Magnetic Ground States of 100 Binary *d*-Metal Oxides Studied by Hybrid Density Functional Methods

Mikhail S. Kuklin, Kim Eklund, Jarno Linnera, Artturi Ropponen , Nikolas Tolvanen and Antti J. Karttunen * 

Department of Chemistry and Materials Science, Aalto University, FI-00076 Aalto, Finland; mikhail.kuklin@aalto.fi (M.S.K.); kim.eklund@aalto.fi (K.E.); jarno.linnera@aalto.fi (J.L.)

* Correspondence: antti.karttunen@aalto.fi

Abstract: *d*-metal oxides play a crucial role in numerous technological applications and show a great variety of magnetic properties. We have systematically investigated the structural properties, magnetic ground states, and fundamental electronic properties of 100 binary *d*-metal oxides using hybrid density functional methods and localized basis sets composed of Gaussian-type functions. The calculated properties are compared with experimental information in all cases where experimental data are available. The used PBE0 hybrid density functional method describes the structural properties of the studied *d*-metal oxides well, except in the case of molecular oxides with weak intermolecular forces between the molecular units. Empirical D3 dispersion correction does not improve the structural description of the molecular oxides. We provide a database of optimized geometries and magnetic ground states to facilitate future studies on the more complex properties of the binary *d*-metal oxides.

Keywords: oxides; transition metals; magnetism; computational chemistry; density functional theory



Citation: Kuklin, M.S.; Eklund, K.; Linnera, J.; Ropponen, A.; Tolvanen, N.; Karttunen, A.J. Structural Properties and Magnetic Ground States of 100 Binary *d*-Metal Oxides Studied by Hybrid Density Functional Methods. *Molecules* **2022**, *27*, 874. <https://doi.org/10.3390/molecules27030874>

Academic Editors: Marek Cypriak and Piotr Paneth

Received: 31 December 2021

Accepted: 24 January 2022

Published: 27 January 2022

Publisher's Note: MDPI stays neutral with regard to jurisdictional claims in published maps and institutional affiliations.



Copyright: © 2022 by the authors. Licensee MDPI, Basel, Switzerland. This article is an open access article distributed under the terms and conditions of the Creative Commons Attribution (CC BY) license (<https://creativecommons.org/licenses/by/4.0/>).

1. Introduction

d-metal oxides play a crucial role in many technological applications [1–8]. In particular, they find use in electronics [2,3,5], thermoelectrics [6,8], and applications related to their magnetic properties [7]. In addition to bulk metal oxide materials, oxide thin films possess unique properties due to their thickness-dependent properties which are widely known in catalysis [1–4]. Many of the *d*-metal oxides are magnetic, which complicates both experimental and computational studies. For example, magnetic structures of the *d*-metal oxides cannot be solved by ordinary X-ray techniques but require neutron diffraction or special techniques such as resonant X-ray scattering. In computational studies, open-shell magnetic compounds pose a challenge for methods based on density functional theory (DFT).

It is well known that DFT methods such as DFT-PBE, where the exchange-correlation functional is based on the generalized gradient approximation (GGA), fail in describing magnetic and electronic structures of strongly correlated *d*-metal oxides, sometimes even leading to a wrong magnetic ground state [9–16]. Even in the case of diamagnetic *d*-metal oxides such as Cu₂O, DFT-GGA may describe the electronic properties rather poorly, resulting in a poor description of other properties such as phonons [17]. These challenges arise from the self-interaction error of DFT-GGA, resulting from the over-delocalization of the electrons in the metal *d* orbitals, in particular 3*d* orbitals [9,18–21]. As a result, the electronic structure can be even qualitatively wrong. This problem can be partially solved by using the Hubbard parameter (*U*) which localizes the electrons on the *d*-metal atoms [22]. However, even GGA + *U* underestimates band gaps of *d*-metal monoxides [18,23]. Furthermore, in addition to the problem with the *d*-metal orbitals, a similar issue with over-delocalization affects the oxygen 2*p* orbitals; in which case, the *U* correction does not help to overcome the problem [24]. Recently, promising results on magnetic La₂CuO₄ and VO₂ were obtained

by meta-GGA DFT-SCAN functional [25–27]. However, at the same time, it was shown that the treatment of the electronic structure of semiconducting and insulating materials by DFT-SCAN are typically not improved over DFT-GGA [28–30].

Hybrid density functionals that incorporate some exact exchange are known to significantly correct the self-interaction error, leading to correct description of the electronic and magnetic structures [15,18,20,21,24,31–33]. In particular, the main improvement of hybrid functionals over GGA functionals is the correct treatment of the valence bands near the Fermi level, leading to correct localization of the electrons [15,21]. The structural and electronic properties are typically described reasonably well, even if the band gap is generally overestimated [34,35]. Approaches to further improve the band gap prediction of hybrid functionals have also been suggested: dielectric-dependent hybrid functionals do not show real improvement, but the application of so-called charge transition level scheme leads to the further improvement of the predicted band gaps [36,37]. In principle, it is possible to tune the band gap predictions by tuning the amount of exact exchange, but such an empirical approach deteriorates the predictive power of the methodology [21]. In general, hybrid functionals with about 25% exact exchange such as PBE0 have been shown to describe *d*-metal oxides and their magnetic structures reasonably well [15,21,24,31]. The screened hybrid functionals such as HSE06 are another very commonly used approach in solid-state DFT studies, and they have been shown to predict band gaps of *d*-metal oxides and dichalcogenides with good accuracy [38].

Even though a vast number of computational studies on binary *d*-metal oxides have been reported in the literature, most of them have included only some subset of the binary *d*-metal oxides, and a comparison of the results is complicated by the variety of used computational methodologies. A comprehensive dataset of the structural properties and magnetic ground states of binary *d*-metal oxides, obtained with a DFT method that can properly describe the electronic structures of strongly correlated oxides, would facilitate future studies on more complex properties and eventual material applications. As an example of data analytics enabled by such datasets, Posysaev et al. recently investigated the oxidation states of a number of binary oxides taken from the AFLOW library [39]. Examples of physical and transport properties that can be nowadays accessed routinely with hybrid DFT methods are elastic, dielectric, piezoelectric, and thermoelectric properties [40].

Here, we present a comprehensive computational investigation of *d*-metal oxides known at the atmospheric pressure by using the hybrid DFT-PBE0 method (see Materials and Methods for computational details). We focus on binary *d*-metal oxides such as Fe₂O₃ and CuO and rule out ternary *d*-metal oxides such as FeTiO₃ or CoTiO₃. We studied in total 100 binary *d*-metal oxides, reporting their structural properties and magnetic ground states, including magnetic ground states at 0 K for materials that were reported to be paramagnetic at room temperature. We also investigate the effect of DFT-D3 dispersion correction on structural properties of molecular *d*-metal oxides [41]. We report the performance of the DFT-PBE0 method for binary *d*-metal oxides and provide a freely available dataset that enables further studies on their spectroscopic, mechanical, dielectric, and transport properties.

2. Results and Discussion

2.1. General Overview of the Results

We considered in total 100 binary *d*-metal oxides that are known to exist at the atmospheric pressure. We distinguished the studied oxides by their structural formula and Pearson symbol. Several *d*-metal oxides have high-temperature polymorphs which were included if they possessed an ordered crystal structure. High-pressure modifications were excluded from the present study. In the main text, we discuss only the magnetic oxides in detail, while results for nonmagnetic oxides are provided in the Supplementary Materials.

Table 1 lists the Pearson symbols, space groups, magnetic ground states, magnetic moments, and band gaps of the studied magnetic *d*-metal oxides. As discussed above, it is known that hybrid DFT methods may typically overestimate band gaps. Furthermore, our

calculated band gaps are for perfect single crystals at 0 K, while the experimental band gaps are typically reported for room temperature and might depend significantly on the sample type (single crystal, polycrystalline, and thin film). Therefore, qualitative comparisons with the experimental results (insulating vs. metallic nature) are here more relevant than quantitative comparisons.

Table 1. Pearson symbols, space groups, magnetic ground states, spin magnetic moments for the metal atoms (μ_B), and band gaps of the studied magnetic binary *d*-metal oxides.

Oxide	Pearson Symbol ^a	Space Group of Nonmagnetic Unit Cell	Space Group of Magnetic Unit Cell	Magnetic Ground State ^b	Magnetic Moment (μ_B) ^c		Band Gap (eV)	
					Calc.	Exp.	Calc.	Exp.
3d metals								
Ti ₂ O ₃	<i>hR10</i>	<i>R-3c</i> (167)	<i>R3c</i> (161)	AFM	0.9		2.7	0.1 [42]
α -Ti ₃ O ₅	<i>oS32</i>	<i>Cmcm</i> (63)	<i>Cm</i> (8)	FiM	1.0		2.0	
β -Ti ₃ O ₅	<i>mS32</i>	<i>C2/m</i> (12)	<i>Cm</i> (8)	AFM	0.9, 1.0		1.3	0.14 [43]
γ -Ti ₃ O ₅	<i>mS32</i>	<i>I2/c</i> (15)	<i>P1</i> (1)	AFM	1.0		2.3	
δ -Ti ₃ O ₅	<i>mS32</i>	<i>P2/a</i> (13)	<i>P-1</i> (2)	AFM	1.0		2.4	0.07 [44]
λ -Ti ₃ O ₅	<i>mS32</i>	<i>C2/m</i> (12)	<i>Cm</i> (8)	AFM	1.0		1.7	
V ₂ O ₃	<i>hR10</i>	<i>R-3c</i> (167)	<i>R3c</i> (161)	AFM/AFM	2.0		3.0	
V ₂ O ₃	<i>mS20</i>	<i>I2/a</i> (15)	<i>P2/c</i> (13)	AFM/AFM	2.0	1.2 [45]	2.8	0.6 [46]
VO ₂	<i>mP12</i>	<i>P2₁/c</i> (14)	<i>P2₁</i> (4)	PM/AFM	1.1		3.0	0.6–0.7 [47]
VO ₂	<i>mS12</i>	<i>C2/m</i> (12)	<i>Cm</i> (8)	PM/AFM	1.1		3.3	
VO ₂	<i>tP6</i>	<i>P4₂/mmm</i> (136)	<i>Cmmm</i> (65)	PM/AFM	1.1		2.8	-
Cr ₂ O ₃	<i>hR10</i>	<i>R-3c</i> (167)	<i>R3c</i> (161)	AFM/AFM	3.0	ca. 2.7 [48]	5.1	3.2–3.4 [49,50]
CrO ₂	<i>tP6</i>	<i>P4/mmm</i> (136)	<i>P4/mmm</i> (136)	FM/FM	2.4	2.01 [51]		
MnO	<i>cF8</i>	<i>Fm-3m</i> (225)	<i>R-3m</i> (166)	AFM/AFM	4.8	4.58 [52]	3.9	3.6–4.2 [53,54]
MnO	<i>hP4</i>	<i>P6₃mc</i> (186)	<i>Pmc2₁</i> (26)	AFM	4.8		3.0	
Mn ₂ O ₃	<i>oP80</i>	<i>Pbca</i> (61)	<i>Pbca</i> (61)	AFM/AFM	3.9, 4.0	2.3–3.9 [55,56]	3.0	2.17 [57], 2.4 [58]
Mn ₂ O ₃	<i>cI80</i>	<i>Ia-3</i> (206)	<i>Ia-3</i> (206)	PM/FM	4.1			
Mn ₃ O ₄	<i>tI28</i>	<i>I4₁/amd</i> (141)	<i>I4₁/amd</i> (141)	FiM/FiM	3.9, 4.0, 4.9		3.2	1.77–2.72 [59]
MnO ₂	<i>tI24</i>	<i>I4/m</i> (87)	<i>C2/m</i> (12)	AFM/AFM	3.1		3.4	1.32 [60]
MnO ₂	<i>oP12</i>	<i>Pnam</i> (62)	<i>Pmc2₁</i> (26)	AFM/AFM	3.0		3.5	2.57 [61]
MnO ₂	<i>tP6</i>	<i>P4/mmm</i> (136)	<i>Cmmm</i> (65)	AFM/AFM	3.1		2.1	0.3 [62]
MnO ₂	<i>cF48</i>	<i>Fd-3m</i> (227)	<i>Imma</i> (74)	AFM/AFM	3.1	2.78 [63]	3.7	1.7–3.5 [64]
Fe ₃ O ₄	<i>cF56</i>	<i>Fd-3m</i> (227)	<i>Fd-3m</i> (227)	FiM/FiM	4.0, 4.2	3.82 [65]		
Fe ₃ O ₄	<i>mP56</i>	<i>P2/c</i> (13)	<i>P2/c</i> (13)	FiM/FiM	3.7–4.3	4.17, 4.44 [66]	1.6	0.14 [11]
Fe ₂ O ₃	<i>hR10</i>	<i>R-3c</i> (167)	<i>R-3</i> (148)	AFM/AFM	4.2	4.6–5.2 [67]	4.0	5.0 [68,69]
Fe ₂ O ₃	<i>cI80</i>	<i>Ia-3</i> (206)	<i>I2₁2₁2₁</i> (24)	AFM/AFM	4.3		3.3	2.2 [70]
Fe ₂ O ₃	<i>oP40</i>	<i>Pna2₁</i> (33)	<i>Pna2₁</i> (33)	FiM/AFM	4.3		4.2	1.6 [71]
CoO	<i>cF8</i>	<i>Fm3m</i> (225)	<i>R-3m</i> (166)	AFM/AFM	2.7	3.35, 3.8 [72,73]	4.5	4.3 [74]
CoO	<i>hP4</i>	<i>P6₃mc</i> (186)	<i>Pmc2₁</i> (26)	AFM	2.8		3.2	
Co ₃ O ₄	<i>cF56</i>	<i>Fd-3m</i> (227)	<i>F-43m</i> (216)	AFM/AFM	2.8	3.88 [75], 3.0 [76]	4.0	0.7 [77]
NiO	<i>cF8</i>	<i>Fm3m</i> (225)	<i>R-3m</i> (166)	AFM/AFM	1.7	1.64 [78], 1.77 [79], 1.90 [52]	5.2	4.0 [80], 4.3 [81]
CuO	<i>mS8</i>	<i>C2/c</i> (15)	<i>P2₁/c</i> (14)	AFM/AFM	0.6	0.65 [82], 0.68 [83,84]	3.8	1.7 [85]
Cu ₄ O ₃	<i>tI28</i>	<i>I4₁/amd</i>	<i>Imma</i> (74)	AFM/AFM	0.7	0.66 [86]	2.9	ca. 1.5 [87]
4d metals								
MoO ₂	<i>mP12</i>	<i>P2₁/c</i> (14)	<i>P2₁</i> (4)	PM/AFM	1.1			
TcO ₂	<i>mP12</i>	<i>P2₁/c</i> (14)	<i>P2₁</i> (4)	PM/AFM	2.7		2.4	
RuO ₂	<i>tP6</i>	<i>P4/mmm</i> (136)	<i>Cmmm</i> (65)	PM/AFM	1.5	0.05 [88]		
RhO ₂	<i>tP6</i>	<i>P4₂/mmm</i> (136)	<i>P4/mmm</i> (136)	PM/FM	0.6			
Ag ₃ O ₄	<i>mP14</i>	<i>P2₁/c</i> (14)	<i>P2₁/c</i> (14)	PM/FM	0.2			
5d metals								
WO ₂	<i>mP12</i>	<i>P2₁/c</i> (14)	<i>P2₁</i> (4)	PM/AFM	0.4			
ReO ₂	<i>mP12</i>	<i>P2₁/c</i> (14)	<i>P2₁</i> (4)	PM/AFM	2.1		1.5	
ReO ₂	<i>oP12</i>	<i>Pbcn</i> (60)	<i>P2₁2₁2</i> (18)	PM/AFM	1.1		1.6	
ReO ₂	<i>tP6</i>	<i>P4₂/mmm</i> (136)	<i>Cmmm</i> (65)	AFM	2.7		1.6	
IrO ₂	<i>tP6</i>	<i>P4₂/mmm</i> (136)	<i>Cmmm</i> (65)	PM/AFM	0.5			

^a Pearson symbol is used for the description of the crystal structure. It includes the Bravais lattice and the number of atoms in the (nonmagnetic) crystallographic unit cell. ^b The ground magnetic state determined in this study (FM: ferromagnetic, AFM: antiferromagnetic, and FiM: ferrimagnetic). In the cases where experimental information on the magnetic ground state is available, the first value is the experimentally determined magnetic ground state, and the second one is the ground state determined here (at 0 K). ^c Magnetic moments of the *d*-metal atoms. The calculated values correspond to atomic spin populations.

The overall performance of the DFT-PBE0/TZVP level of theory in reproducing lattice constants of the magnetic binary d -metal oxides is illustrated in Figure 1. In the lattice parameter comparisons for magnetic structures, the nonmagnetic experimental unit cell has been transformed so that it corresponds to the calculated magnetic unit cell. All reported magnetic moments are spin-only values without any orbital contributions, which can lead to some deviations from experimentally determined magnetic moments.

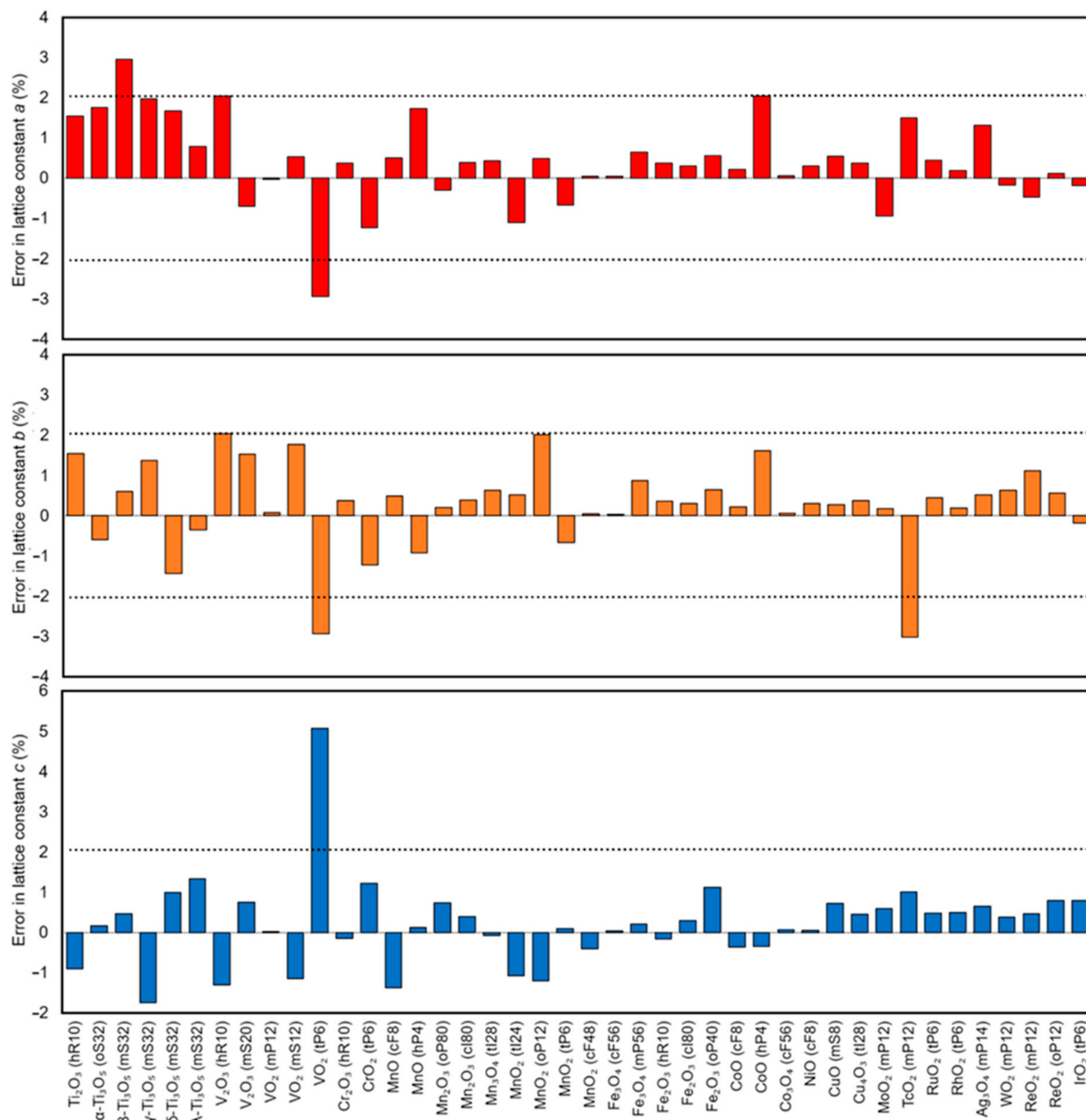


Figure 1. Errors in the optimized DFT-PBE0/TZVP lattice constants in comparison with the experimental lattice constants of the studied magnetic d -metal oxides. ReO₂ ($tP6$) is not included in the plot (see text for details).

Generally, the DFT-PBE0/TZVP level of theory describes the structures of the studied magnetic d -metal oxides with good accuracy: mean absolute error (MAE) of the optimized lattice constants is 0.8%, and mean error (ME) is 0.3%. For comparison, using a smaller SVP basis set results in MAE of 0.9% and ME of 0.1%. The smaller SVP basis set thus appears

to benefit from some cancellation of errors. For the whole set of the structures, including nonmagnetic *d*-metal oxides, MAE is 1.1% for TZVP basis set and 1.0% SVP basis sets, while ME is 0.6% for TZVP and 0.3% for SVP. The following metal oxides with abnormally large errors of more than 10% in the lattice constants are omitted in these statistics as outliers and discussed in the text: ReO₂ (*tP6*), HgO₂ (*mS6*), and HgO₂ (*oP12*).

Out of the magnetic metal oxides investigated here, 16 are described in the literature as antiferromagnets. We were able to find an antiferromagnetic ground state for all of them. The antiferromagnetic configuration was described in the literature in full detail for 12 out of the 16 AFM oxides, and our results reproduced all these reported configurations, except for the helical configuration of MnO₂ (*tP6*) or β-MnO₂. Of the four systems that are ferrimagnetic according to the literature, three had the ferrimagnetic lowest-energy configurations, but for one (Fe₂O₃ *oP40* or ε-Fe₂O₃), we found an antiferromagnetic ground state. Our ground state gives the same magnetic configuration as reported for the ferrimagnet, but the magnetic moments do not have values matching the ferrimagnetic configuration. The one experimentally ferromagnetic oxide (CrO₂) was also reproduced. Of the 13 paramagnetic systems, our results predict an antiferromagnetic 0 K configuration for 10 and ferromagnetic for three oxides.

Concerning the predicted band gaps, DFT-PBE0 shows behavior that has been previously discussed in detail in the literature [33]. For systems where the experimental band gap is smaller than 1 eV, DFT-PBE0 typically significantly overestimates the band gap. This is evident especially in the case of titanium and vanadium oxides studied here. For band gaps between 2 and 5 eV, DFT-PBE0 produces more reasonable estimates. The comparisons of experimental and calculated band gaps are complicated by the fact that material defects such as vacancies can affect the band gap of the oxides significantly. Metal oxides often show, for example, nonstoichiometry, and some oxides such as TiO were even excluded from the study due to their significant nonstoichiometry. Finally, the band gaps discussed here were obtained simply as the fundamental 0 K energy gap between the highest occupied and lowest unoccupied bands, and both excitonic and finite temperature effects were neglected. It would, in principle, be possible to improve the agreement with experiments by tuning what is among the exact exchange for each material, but we avoided any empirical parametrization to obtain an overview of the performance of nonempirical PBE0 across the whole *d*-block.

We first discuss the results for the binary *3d* metal oxides, followed by *4d* and *5d* oxides. Within each period, the *d*-metal oxides are discussed in order from group 3 to group 12. Additionally, we separately discuss molecular *d*-metal oxides and several mercury oxides.

Some binary *d*-metal oxides were excluded based on the following reasons: La₂O₃ (Pearson symbol *hP5*) is a high-T phase stable at > 2303 K and has occupancy of 0.5 at all sites; La₂O₃ (*cI5*) has an occupancy of 0.5 for oxygen atoms; TiO (*mS20*) and TiO (*cF8*) are nonstoichiometric; VO (*cF8*) is nonstoichiometric; ε-MnO₂ (*hP3*) has 0.5 occupancy on Mn sites; in the case of Fe₃O₄ (*mS224*), the reduced structure Fe₃O₄ (*mP56*) was calculated instead; γ-Fe₂O₃ (*cP56*) has occupancy of 0.35 at a Fe site; MoO₃ (*mP16*) has 0.5 occupancy on several sites; and TaO₂ (*tP6*) is nonstoichiometric.

2.2. Magnetic Binary 3D-Metal Oxides

Six of the studied titanium oxides are magnetic (Figure 2). Ti(III) oxide, Ti₂O₃ (*hR10*), adopts the trigonal corundum structure with space group *R-3c* (no. 167) [89]. Taking the magnetic structure into account changes the space group to subgroup *R3c* (161) (Figure 2a). There are no experimental data on the magnetic nature of Ti₂O₃. We found the AFM configuration to be the ground state of Ti₂O₃ with magnetic moments of 0.9 μ_B, whereas previous calculations by the screened exchange hybrid DFT described Ti₂O₃ as a diamagnetic structure [90]. In the same paper, it was mentioned that the ground state of the Ti₂O₃ is experimentally determined to be diamagnetic at a low temperature. The lattice parameters of the calculated Ti₂O₃ (*hR10*) match the experimental values well with a difference of +1.6% for *a* and −0.9% for *c*. The calculated band gap of 2.7 eV is clearly overes-

timated compared to the experimental value of 0.1 eV [42]. However, harmonic frequency calculations performed on the structure revealed imaginary frequencies. Scanning along the imaginary modes reduced the symmetry of the antiferromagnetic structure to space group $C1c1$ (no. 9). This structure was also observed to be energetically more favorable than the higher symmetry one (by about 2 kJ/mol per atom), with a band gap of 2.5 eV and magnetic moment of $1.0 \mu_B$.

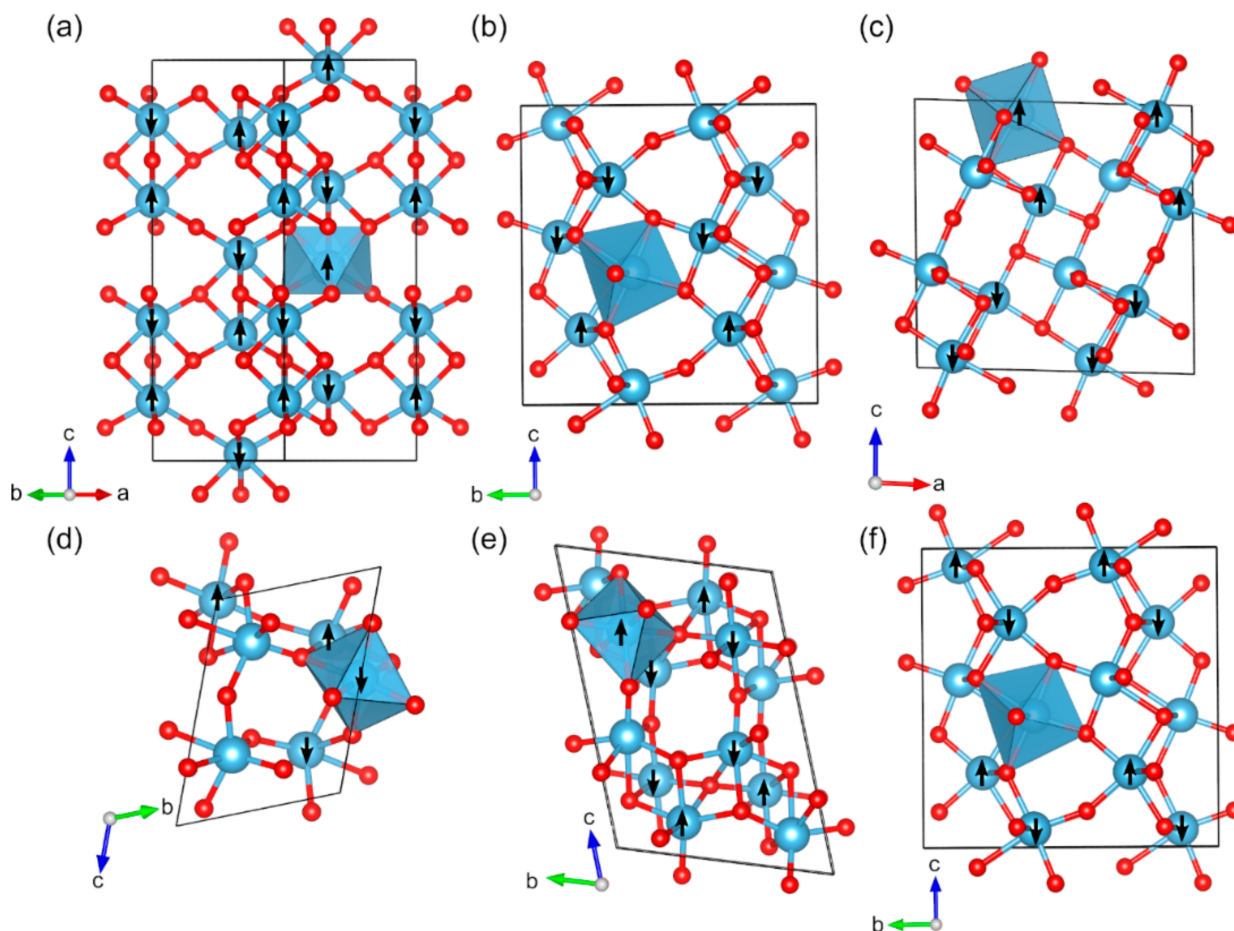


Figure 2. Optimized structures of studied magnetic binary titanium oxides (red: O, blue: Ti): (a) Ti_2O_3 (*hR10*), (b) $\alpha-Ti_3O_5$ (*oS32*), (c) $\beta-Ti_3O_5$ (*mS32*), (d) $\gamma-Ti_3O_5$ (*mS32*), (e) $\delta-Ti_3O_5$ (*mS32*), and (f) $\lambda-Ti_3O_5$ (*mS32*). The directions of the magnetic moments are illustrated by black arrows. Coordination octahedra of Ti atoms are shown in blue color.

Ti(III/IV) oxide, $\alpha-Ti_3O_5$, (*oS32*) crystallizes in an orthorhombic crystal structure with space group $Cmcm$ (no. 63) (Figure 2b) [91]. Taking the magnetic ordering into account changes the space group to the subgroup Cm (8). $\alpha-Ti_3O_5$ exists at temperatures higher than 460 K, while below 460 K it transforms to $\beta-Ti_3O_5$. There is little experimental data available on the magnetic and electronic properties of $\alpha-Ti_3O_5$. The lattice parameters are described with good accuracy compared to the experiment: the calculated lattice constants differ from the experimental values by +1.8% for a , $-0.6%$ for b , and +0.2% for c . We identified ferrimagnetic spin-ordering for $\alpha-Ti_3O_5$ with magnetic moments of $1.0 \mu_B$ for some Ti^{3+} atoms and nonmagnetic Ti^{4+} (Table 1). The calculated band gaps (2.0 eV) cannot be compared with the literature as there are no previous experimental or computational data, but the material has been reported to be a semiconductor [92].

$\beta-Ti_3O_5$ (*mS32*) adopts monoclinic crystal structure with space group $C2/m$ (no. 12) [93]. For the magnetic ordering, the space group is changed to the subgroup Cm (8) (Figure 2c). We found an antiferromagnetic configuration with magnetic moments of 0.9 and $1.0 \mu_B$

on Ti^{3+} atoms to be the most favorable energetically, whereas no experimental data are available on the magnetic ordering. Based on our calculations, $\beta\text{-Ti}_3\text{O}_5$ (*mS32*) is an insulator with a band gap of 1.3 eV, compared to experimentally measured 0.14 eV [43]. In comparison to the experiment, the optimized lattice constants of the $\beta\text{-Ti}_3\text{O}_5$ (*mS32*) show differences of +3.0% for *a*, +0.6% for *b*, and +0.5% for *c*.

Another Ti(III/IV) oxide, $\gamma\text{-Ti}_3\text{O}_5$ (*mS32*), has a monoclinic crystal structure with space group *I2/c* (15) (Figure 2d) [44]. $\gamma\text{-Ti}_3\text{O}_5$ is formed from $\beta\text{-Ti}_3\text{O}_5$ at ~250 K and further transforms to $\delta\text{-Ti}_3\text{O}_5$ below 237 K [94]. Based on our calculations, $\gamma\text{-Ti}_3\text{O}_5$ is an insulator with band gap of 2.3 eV, whereas it has been reported to be metallic based on the experimental data [44]. By studying different magnetic configurations, we found that antiferromagnetic $\gamma\text{-Ti}_3\text{O}_5$ (*mS32*) is the most favorable configuration, energetically speaking. The magnetic ground state has four Ti^{3+} atoms with localized spins and two nonmagnetic Ti^{4+} atoms (Table 1). In comparison to the experiment, the optimized lattice constants of $\gamma\text{-Ti}_3\text{O}_5$ (*mS32*) show differences of +2.0%, +1.4%, and -1.7% for *a*, *b*, and *c*, respectively.

$\delta\text{-Ti}_3\text{O}_5$ (*mS32*) adopts monoclinic crystal structure with space group *P2/a* (no. 13) [44]. The space group of the magnetically ordered structure is *P-1* (no. 2) (Figure 2e). Based on our calculations, $\delta\text{-Ti}_3\text{O}_5$ (*mS32*) is an insulator with a band gap of 2.4 eV, and clearly overestimated compared to 0.07 eV from experimental studies [44]. The lattice parameters compare well with experimentally known crystal structure, with differences of 1.7% for *a*, -1.4% for *b*, and 1.0% for *c*. As for other Ti_3O_5 phases, there are no experimental data on magnetic moments of $\delta\text{-Ti}_3\text{O}_5$ (*mS32*), but it is estimated to be $1.0 \mu_{\text{B}}$ for Ti^{3+} atoms.

Recently, synthesis of a new structure, $\lambda\text{-Ti}_3\text{O}_5$ (*mS32*) was reported that crystallizes in monoclinic crystal structure with space group *C2/m* (no. 12) [43]. We found antiferromagnetic configuration to be the energetically most favorable for $\lambda\text{-Ti}_3\text{O}_5$ (*mS32*), arising from magnetically ordered structure in subgroup *Cm* (no. 8) (Figure 2f). Calculated magnetic moments are $1.0 \mu_{\text{B}}$ for Ti^{3+} atoms. Even though experimentally the material was reported to be metallic, our calculations showed band gap of 1.7 eV. Such discrepancy may be due to the experimental conditions: a photoreversible metal-semiconductor phase transition. Also, nanoparticles (ca. 25 nm.) were studied and the results can be different compared to single-crystalline bulk material. The optimized lattice constants of $\lambda\text{-Ti}_3\text{O}_5$ (*mS32*) differ from experimental data by +0.8% for *a*, -0.3% for *b*, and 1.3% for *c*.

For vanadium, we investigated five magnetic binary oxides (Figure 3). Two V(III) oxides are known: V_2O_3 (*hR10*) and V_2O_3 (*mS20*). V_2O_3 (*hR10*) is stable above 155 K and V_2O_3 (*mS20*) below 155 K [95]. The V_2O_3 (*hR10*) modification crystallizes in the trigonal corundum structure with space group *R-3c* (no. 167) and has been described in detail in a recent DFT study [31,69,95–97]. V_2O_3 (*mS20*) has a monoclinic crystal structure with space group *I2/a* (no. 15) [45,98]. In line with experimental data, the magnetic ground state of V_2O_3 (*mS20*) was found to be AFM configuration with a calculated spin magnetic moment of $2.0 \mu_{\text{B}}$ (exp. value $1.2 \mu_{\text{B}}$) (Table 1). The AFM ground state can be realized in the subgroup *P2c* (no. 13) (Figure 3a). Optimized lattice parameters match the experimental values with good accuracy, lattice parameters differing by -0.7% , +1.5%, and +0.8% for *a*, *b*, and *c*, respectively. The calculated band gap is 2.8 eV, while a clearly smaller gap of 0.6 eV has been reported experimentally [46].

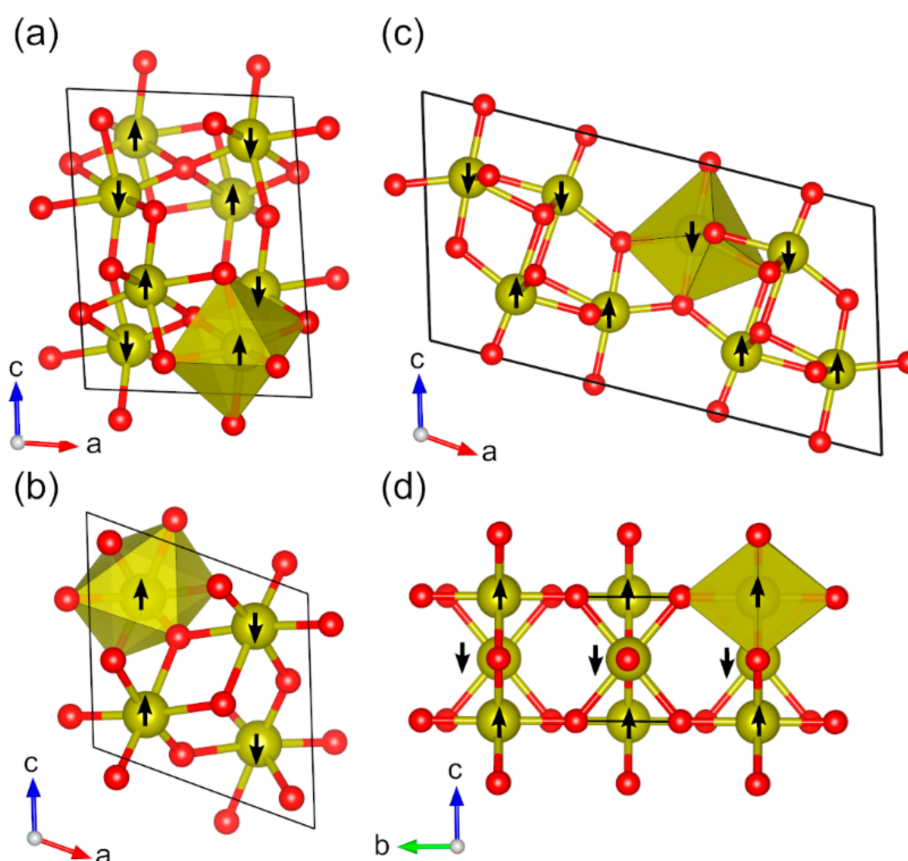


Figure 3. Optimized structures of studied magnetic binary vanadium oxides (red: O, yellow: V): (a) V_2O_3 (*mS20*), (b) VO_2 (*mP12*), (c) VO_2 (*mS12*), and (d) VO_2 (*tP6*). The directions of magnetic moments are illustrated by black arrows. Coordination octahedra of V atoms are shown in yellow color.

Three different VO_2 modifications are known: VO_2 (*mP12*), VO_2 (*mS12*), and VO_2 (*tP6*) [99,100]. VO_2 (*mP12*) crystallizes in the space group $P2_1/c$ (no. 14), the symmetry being lowered to subgroup $P2_1$ (no. 4) for the magnetically ordered structure (Figure 3b). VO_2 (*mS12*) has a monoclinic crystal structure with space group $C2/m$ (no. 12), while taking the magnetic ordering into account lowers the symmetry to subgroup Cm (no. 8) (Figure 3c). The tetragonal VO_2 (*tP6*) modification crystallizes in the space group $P4_2/mnm$ (no. 136), and subgroup $Cmmm$ (no. 65) was used to describe the magnetic ordering (Figure 3d).

Overall, all three VO_2 modifications have been experimentally characterized to be paramagnetic [101]. VO_2 (*mP12*) is stable below 340 K, while VO_2 (*tP6*) is a high-temperature modification that is stable above 340 K. Experimentally, the high-temperature VO_2 (*tP6*) modification was found to be metallic, whereas our 0 K calculations show a 2.8 eV band gap [99]. In line with the experimental data, we found VO_2 (*mP12*) to be lower in energy compared to VO_2 (*tP6*) at 0 K (by 1.4 kJ mol⁻¹ per atom) [102]. The calculated band gap of VO_2 (*mP12*) is 3.0 eV, whereas experimentally it is estimated to be ca. 0.6–0.7 eV (Table 1). VO_2 (*mS12*) is known to be stable at high pressure and at a zero-strain triple point at 338 K [103]. The lattice constants differ from experimental values by 0.0%, +0.1%, and 0.4% for VO_2 (*mP12*) and by +0.5%, +1.8%, and −1.1% for VO_2 (*mS12*). VO_2 (*tP6*) modification shows relatively large differences of −2.9% for *a* and *b* and 5.1% for *c* compared to experimental data. This is likely due to the fact the VO_2 (*tP6*) is a high-temperature modification. Magnetic moments of VO_2 (*mP12*) were reported in a computational study to be $-1 \mu_B$, which is in line with our calculated value of $1.1 \mu_B$ (Table 1) [104].

In the case of chromium, we investigated two magnetic binary oxides. Cr(III) oxide, Cr_2O_3 (*hR10*), crystallizes in the corundum structure type with space group $R-3c$ (no. 167) [48]. Cr_2O_3 (*hR10*) adopts an AFM spin configuration below the Neel temperature

of 309 K, and the magnetically ordered structure in subgroup $R3c$ (no. 161) is identical to Ti_2O_3 ($hR10$) shown in Figure 2a. The lattice constants of the optimized structure match the experimental data well, with a difference of less than 0.5%. The calculated band gap is 5.1 eV, which is larger in comparison with 3.2–3.4 eV from experimental measurements (Table 1). The magnetic moments of the AFM structure are in good agreement with experimental data ($3.0 \mu_B$ calc. and $2.7 \mu_B$ exp.).

Cr(IV) oxide, CrO_2 ($tP6$), crystallizes in the rutile structure type with space group $P4_2/mnm$ (no. 136) [105]. The magnetic structure is known to be ferromagnetic with a Curie temperature of 386.5 K (Figure 4), and the material is known to be a metallic conductor [105–108]. The calculated magnetic moment is in good agreement with the experimental value ($2.4 \mu_B$ calc. vs. $2.01 \mu_B$ exp.) (Table 1), and the lattice parameters of the optimized structure are in line with experimental data (a and c differ by +1.2%).

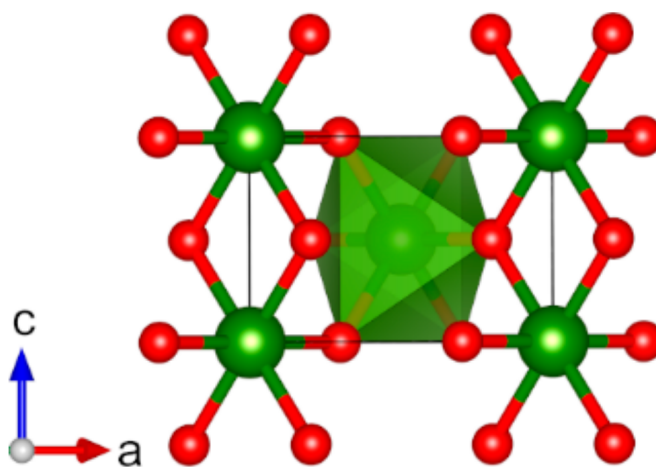


Figure 4. Optimized structure of CrO_2 ($tP6$) (red: O, green: Cr). Spins are aligned along c axis and not visualized. Coordination octahedron of Cr is shown in green color.

For manganese, we studied nine magnetic binary oxides (Figure 5). Mn(II) oxide, MnO ($cF8$), crystallizes in the rock salt structure type with space group $Fm-3m$ (225). For the magnetically ordered structure, the symmetry is reduced to subgroup $R-3m$ (no. 166) (Figure 5a) [74]. The magnetic ground state of MnO is known to be AFM with a Néel temperature of about 122 K [109]. The lattice parameters of the calculated MnO ($cF8$) structure are in good agreement with experimental data: the difference is +0.5% and -1.4% for a and c , respectively. The calculated magnetic moment, $4.8 \mu_B$, is in line with the experimental value of $4.58 \mu_B$ (Table 1), and the calculated band gap is also in the range of experimentally measured band gaps (3.9 eV calc. and 3.6–4.2 eV exp.). Hexagonal polymorph of MnO crystallizes in the wurtzite structure type with space group $P6_3mc$ (186). The magnetic ground state has not been experimentally determined, but previous computational studies report an antiferromagnetic structure [110,111]. The space group symmetry of our calculated antiferromagnetically ordered structure is reduced to subgroup $Pmc2_1$ (no. 26). The calculated band gap of 3.0 eV is smaller than that of the cubic polymorph, while the magnetic moment is the same at $4.8 \mu_B$. Lattice parameter differences are +1.7% for a , -0.9% for b , and +0.1% for c .

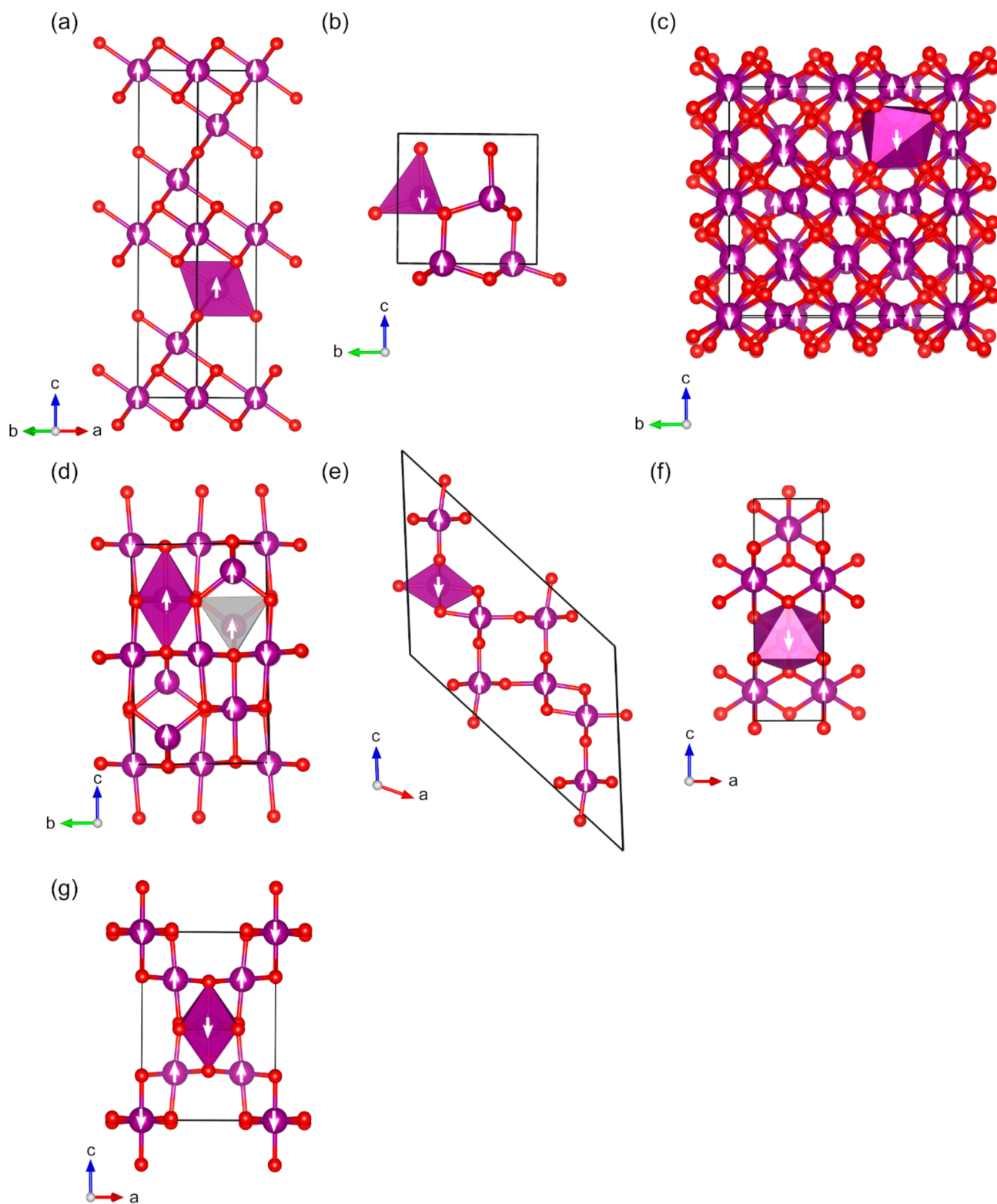


Figure 5. Optimized structures of studied magnetic binary manganese oxides red, O; violet: Mn: (a) MnO (*cF8*), (b) MnO (*hP4*), (c) Mn₂O₃ (*oP80*), (d) Mn₃O₄ (*tI28*), (e) MnO₂ (*tI24*), (f) MnO₂ (*oP12*), and (g) MnO₂ (*cF48*). The directions of magnetic moments are illustrated by white arrows. Coordination octahedra and tetrahedra of Mn atoms are shown in violet and light grey colors, respectively.

Two magnetic Mn(III) oxides are known: Mn_2O_3 (*oP80*) and Mn_2O_3 (*cI80*) [112,113]. The space groups of Mn_2O_3 (*oP80*) and Mn_2O_3 (*cI80*) are *Pbca* (no. 61) and *Ia-3* (no. 206), respectively. Orthorhombic Mn_2O_3 (*oP80*) is stable below 302 K, and above this temperature, the cubic Mn_2O_3 (*cI80*) modification becomes more stable. Only Mn_2O_3 (*oP80*) is shown in Figure 5c as the structures look very similar and only differ by the magnetic ordering. Mn_2O_3 (*oP80*) is experimentally known to be antiferromagnetic, whereas Mn_2O_3 (*cI80*) is considered to be paramagnetic [55,56,114]. Based on our calculations, the Mn_2O_3 (*cI80*) prefers a ferromagnetic spin configuration at 0 K (Table 1). The lattice parameters are described with good accuracy: the difference between the optimized and experimental lattice constants is less than 0.7%. A direct comparison of the electronic structure of the Mn_2O_3 modifications with experiments is not possible due to the absence of experimental data on bulk materials. Band gaps of Mn_2O_3 (*oP80*) were estimated to be 2.17 and 2.4 eV for nanoparticles and thin films, respectively, whereas our calculated band gap is 3.0 eV [57,58]. Based on our calculations, Mn_2O_3 (*cI80*) is a metallic conductor, whereas some experimental studies of nanostructured modifications suggest that the material possesses a band gap (1.24 or 1.8 eV) [57,115]. In this case, however, it is difficult to compare the results as the experimental studies also found that the band gap of Mn_2O_3 (*cI80*) is directly correlated with the size of the nanoparticles (increased size leads to a smaller band gap). Experimentally measured magnetic moments are only available for Mn_2O_3 (*oP80*), and they have been reported as 2.3–3.9 μ_B (calculated values are 3.9 and 4.0 μ_B).

Mn(II/III) oxide, Mn_3O_4 (*tI28*), has a tetragonal crystal structure with space group *I4₁/amd* (no. 141) (Table 1) [116]. Mn_3O_4 is known to adopt a ferrimagnetic spin configuration at the room temperature, with the magnetically ordered structure having space group *Imma* (no. 74) (Figure 5d) [117]. The lattice parameters of the optimized structure are larger than the experimental values only by +0.4%, +0.6%, and −0.1% for *a*, *b*, and *c*, respectively. There is no experimental information available on the magnetic moments, but our results are in good agreement with a previously reported computational studies [118,119]. The band gap of Mn_3O_4 nanoparticles was found to be in range of 1.77–2.72 eV depending on the size, whereas our calculated bulk band gap is 3.2 eV [59].

For Mn(IV), we studied four polymorphs: MnO_2 (*tI24*), MnO_2 (*oP12*), MnO_2 (*tP6*), and MnO_2 (*cF48*) [120–123]. MnO_2 (*tI24*), also known as α - MnO_2 , crystallizes in space group *I4/m* (no. 87), and for the magnetically ordered structure, the symmetry is lowered to space group *C2/m* (no. 12) (Figure 5e). MnO_2 (*oP12*) polymorph (γ -/*R*- MnO_2) adopts an orthorhombic structure with space group *Pnam* (no. 62), with a magnetically ordered structure in space group *Pmc2₁* (no. 26) (Figure 5f). MnO_2 (*tP6*) (β - MnO_2) crystallizes in the rutile structure type, space group *P4₂/mnm* (136), and the magnetic structure in the space group *Cmmm* (no. 65) (identical to VO_2 (*tP6*), Figure 3d). MnO_2 (*cF48*) (λ - MnO_2) crystallizes in the cubic space group *Fd-3m* (227), whereas the magnetic structure is orthorhombic with space group *Imma* (no. 74) (Figure 5g). The lattice parameters of the optimized structures match the experimental data very well: the typical difference between calculated and experimental lattice constants is less than 1%. MnO_2 (*tP6*) possesses a helical magnetic configuration below 92 K [56,124,125], whereas all other polymorphs are antiferromagnetic (the Néel temperatures of MnO_2 (*tI24*) and MnO_2 (*cF48*) are 24.5 and 32 K, respectively) [63,126,127]. The only available experimentally measured magnetic moments are for MnO_2 (*cF48*): 3.1 μ_B calc. compared to 2.78 μ_B exp. (Table 1). The data on band gaps of bulk structures are also very limited, and we only found a gap of 0.3 eV reported for MnO_2 (*tP6*) (2.1 eV calc.). The band gap of thin films of MnO_2 (*cF48*) was estimated from the experiment to be in the range of 1.7–3.5 eV, while the calculated band gap for the bulk structure is 3.7 eV [64]. The band gap of nanoflakes of MnO_2 (*oP12*) was estimated to be 2.57 eV, whereas the calculated bulk band gap is 3.5 eV [61].

For iron, we investigated five magnetic binary oxides. Two Fe(II/III) oxides are known: Fe_3O_4 (*cF56*) and Fe_3O_4 (*mP56*) [66,128]. Fe_3O_4 (*cF56*) crystallizes in space group *Fd-3m* (no. 227) (Figure 6a) and Fe_3O_4 (*mP56*) in space group *P2/c* (no. 13) (Figure 6b). Fe_3O_4 (*mP56*), which is stable below 125 K, is involved in the Verwey transition below 125 K from

the cubic structure [129]. The lattice constants of the optimized Fe_3O_4 (*cF56*) structure exactly reproduce experimental values, whereas the Fe_3O_4 (*mP56*) shows differences of +0.6%, +0.9%, and +0.2% for *a*, *b*, and *c*, respectively. Fe_3O_4 (*cF56*) is known to be ferrimagnetic at the room temperature, and it is a metallic conductor [11,128,130]. Fe_3O_4 (*mP56*) is also a ferrimagnet [66]. Calculated atomic magnetic moments ($4.0/4.2 \mu_B$ for *cF56* and $3.7\text{--}4.3 \mu_B$ for *mP56*) are in good agreement with the experimental values ($3.82 \mu_B$ for *cF56* and 4.17 and $4.44 \mu_B$ exp. for *mP56*). The calculated band gap of Fe_3O_4 (*mP56*) is overestimated by being 1.6 eV in comparison to the experimentally determined 0.1 eV (Table 1).

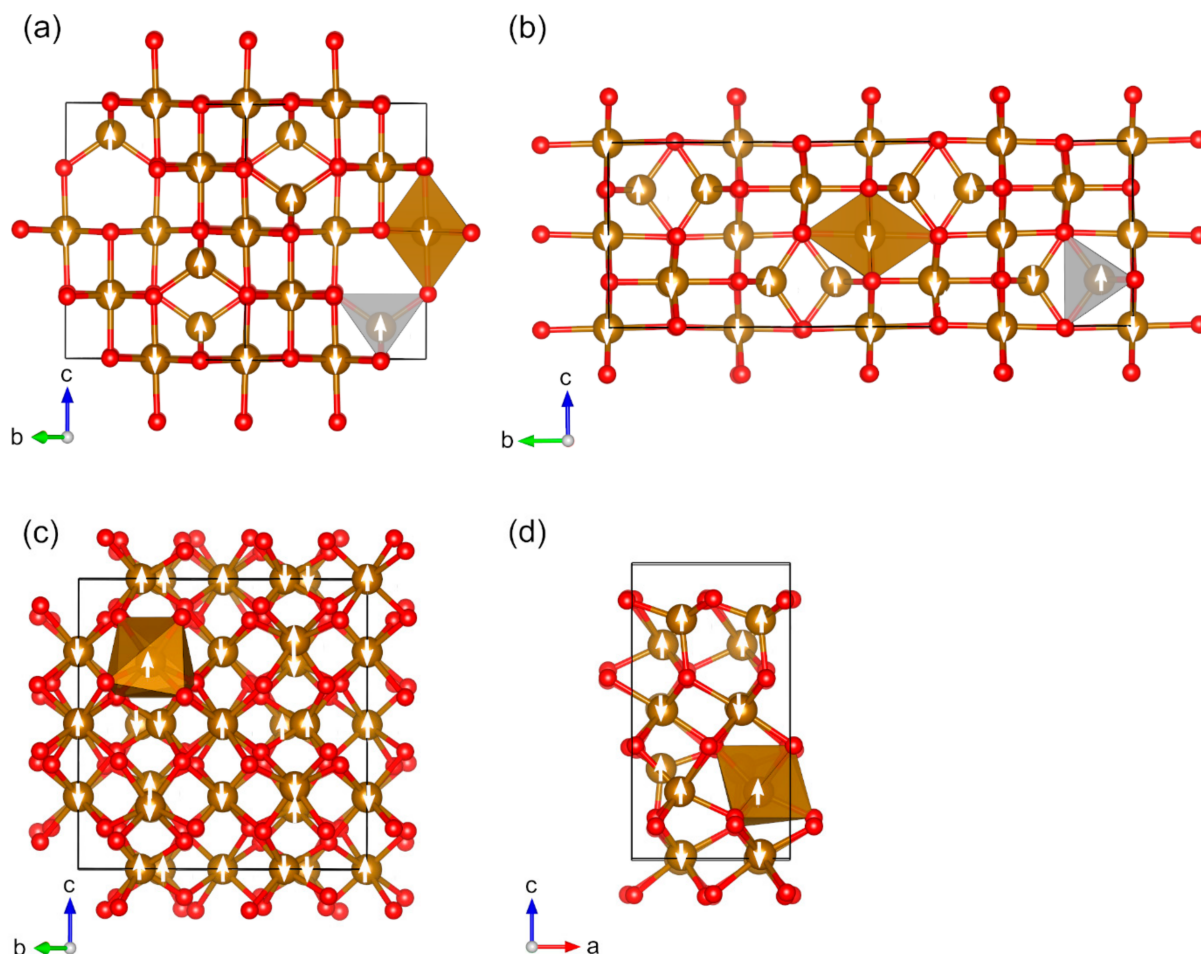


Figure 6. Optimized structures of studied magnetic binary iron oxides (red: O, brown: Fe): (a) Fe_3O_4 (*cF56*), (b) Fe_3O_4 (*mP56*), (c) Fe_2O_3 (*cI80*), and (d) Fe_2O_3 (*oP40*). The directions of magnetic moments are illustrated by white arrows. Coordination octahedra and tetrahedra of Fe atoms are shown in brown and light-grey colors, respectively.

We investigated three Fe(III) oxides: Fe_2O_3 (*hR10*), Fe_2O_3 (*cI80*), and Fe_2O_3 (*oP40*) [68,131,132]. The calculated lattice constants are in the good agreement with experimental values, with the largest difference being 0.9%. Fe_2O_3 (*hR10*), hematite or $\alpha\text{-Fe}_2\text{O}_3$, is known to be antiferromagnetic with the Neel temperature of 955 K, and it has been described in detail in a recent computational study [31]. It crystallizes in the space group *R-3c* (no. 167), whereas the symmetry of the magnetically ordered structure is lowered to space group *R-3* (no. 148). Fe_2O_3 (*cI80*), $\beta\text{-Fe}_2\text{O}_3$, is also known to be antiferromagnetic [133,134]. The space group of the AFM ground state is *1a-3* (no. 206), and the Neel temperature is 119 K (Figure 6c). To our knowledge, there are no experimental data available on the magnetic moments of Fe_2O_3 (*cI80*). The calculated band gap is overestimated to be 3.3 eV compared to the experimental value of 2.2 eV (Table 1). Fe_2O_3 (*oP40*), $\epsilon\text{-Fe}_2\text{O}_3$, is ferrimagnetic with a Curie

temperature of 495 K [135]. However, we found the antiferromagnetic configuration to be the energetically most favorable configuration (ferromagnetic configurations were 2.6–4.7 kJ mol⁻¹ per atom higher in energy, see Supplementary Materials). Spins are correctly aligned in the structure, but Fe atoms in the tetrahedral sites have smaller magnetic moments than they would in a ferrimagnetic configuration. The space group of Fe₂O₃ (*oP40*) is *Pna2*₁ (no. 33), and the magnetically ordered structure has the same space group (Figure 6d). The calculated band gap is estimated to be 4.2 eV, which is clearly overestimated in comparison to the experimental value being 1.6 eV. A comparison of estimated magnetic moments is not feasible as values are only available for nanoparticles.

Co(II) oxide, CoO (*cF8*), crystallizes in the rocksalt structure with space group *Fm-3m* (no. 225) [72–74]. Similar to MnO (*cF8*), the space group of the magnetically ordered structure is *R-3m* (no. 166). CoO (*cF8*) is described in detail in recent computational studies [31,136]. The hexagonal wurtzite polymorph of CoO, *P63mc* (no. 186), has an antiferromagnetic structure similar to hexagonal MnO [137], with the magnetical ordering lowering the space group to *Pmc2*₁ (no. 26). The calculated band gap is 3.2 eV, which is smaller than the value of 4.5 eV of the cubic polymorph. The magnetic moment is 2.8 μ_B. The lattice parameter differences compared to experiments are +2.0% for *a*, +1.6% for *b*, and −0.3% for *c*. Co(II/III) oxide. Co₃O₄ (*cF56*) has a cubic structure with space group *Fd-3m* (no. 227) [138]. The magnetic structure is antiferromagnetic with space group *F-43m* (no. 216) and shows a Neel temperature of 30 K (Figure 7) [75]. The lattice constants are almost identical to the experimental values with a difference of only 0.1%. The calculated magnetic moments of Co²⁺, 2.8 μ_B, reproduce at least one reported experimental value of 3.0 μ_B (Table 1). The reports on Co₃O₄ band gap show a large variation from 0.74 even up to 4.4 eV, with the most recent studies suggesting a fundamental gap of about 0.8 eV [13,77]. Our calculated band gap of 4.0 eV is clearly overestimated in comparison to the values of less than the 1 eV suggested in recent studies. Singh et al. have shown that the electronic and magnetic properties of Co₃O₄ are very sensitive to the choice of the Hubbard parameter (for PBE + *U*_{eff}) and the amount of exact exchange included in the HSE06 hybrid functional [13]. Other computational studies have also shown that the DFT+*U* calculations with *U* values calibrated to the experimental data are required to obtain a good agreement with experimental band gaps [139,140]. Co₃O₄ appears to be a very good benchmark case for any new nonempirical DFT methods.

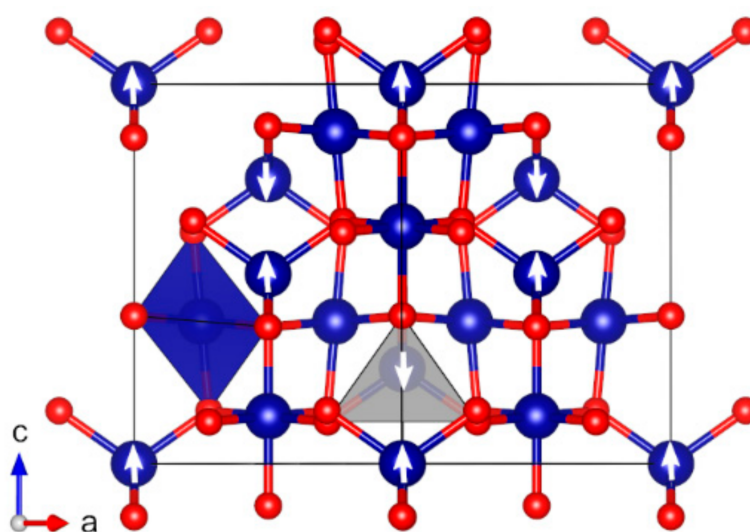


Figure 7. Optimized structure of Co₃O₄ (*cF56*) (red: O, dark blue: Co). The directions of magnetic moments are illustrated by white arrows. Coordination octahedra and tetrahedra of Co atoms are shown in dark-blue and light-grey colors, respectively.

Nickel(II) oxide, NiO (*cF8*), crystallizes in the rocksalt structure, and it has a similar antiferromagnetic structure as MnO (*cF8*) and CoO (*cF8*) [52,74,141,142]. NiO (*cF8*) is described in detail in recent computational studies [31,136].

Copper(II) oxide, CuO (*mS8*), is known to have a monoclinic structure with space group *C2/c* (no. 15) and antiferromagnetic ground state [82–84,143,144]. The space group of the magnetic structure is *P2₁/c* (no. 14), and the structure is described in detail in previous computational studies [31,35]. Copper(I/II) oxide, Cu₄O₃ (*tI28*), crystallizes in a tetragonal crystal structure with space group *I4₁/amd* (no. 141), with the symmetry of the magnetic structure being reduced to the subgroup *Imma* (no. 74) (Figure 8) [145,146]. Cu₄O₃ (*tI28*) is known to be stable as an antiferromagnetic structure with the Neel temperature of 41 K [86]. Whereas the band gap of the optimized structure is overestimated compared with experimentally estimated (2.9 eV. calc. vs. −1.5 eV. exp.), the calculated magnetic moments of Cu²⁺ (0.7 μ_B) are almost identical to experimental value of 0.66 μ_B. The lattice parameters of the optimized structure also match the experimental data well, with differences of less than 0.5%.

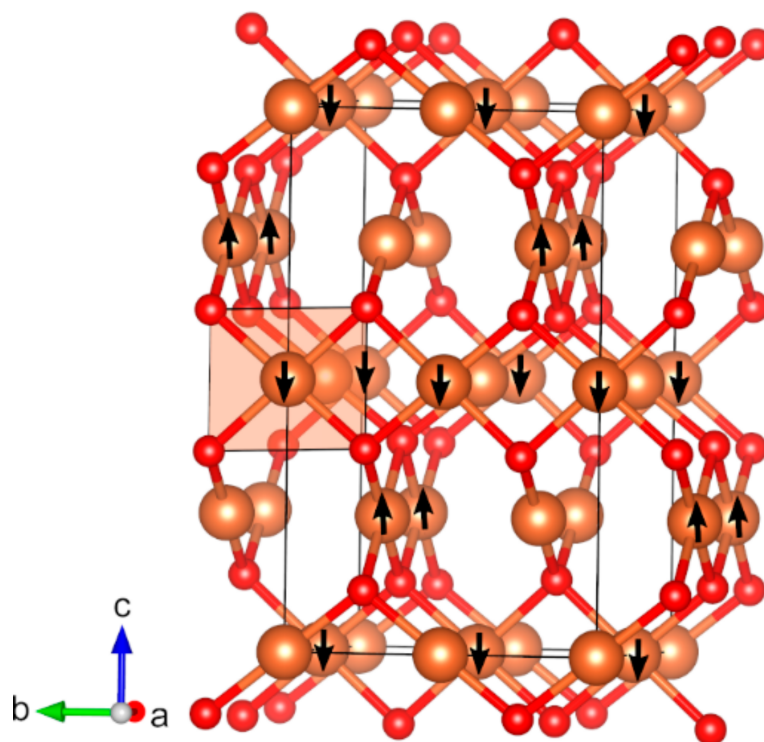


Figure 8. Optimized structure of Cu₄O₃ (*tI28*) (red: O, light brown: Cu). The directions of magnetic moments are illustrated by black arrows. Coordination square planar of Cu atoms that are shown is a light-brown color.

2.3. Magnetic Binary 4D-Metal Oxides

Mo(IV) oxide, MoO₂ (*mP12*), crystallizes in a monoclinic crystal structure with space group *P2₁/c* (no. 14) [147]. It has been determined to be paramagnetic at room temperature [148,149]. We found an antiferromagnetic configuration to possess the lowest energy at 0 K for MoO₂ (*mP12*) (identical to VO₂ (*mP12*) and shown in Figure 3b). Therefore, the symmetry of the magnetic configuration is reduced to subgroup *P2₁* (no. 4). MoO₂ (*mP12*) is a metallic conductor [148]. The lattice parameters of the optimized MoO₂ (*mP12*) are in good agreement with the experimental data, with the differences < 1%. Estimated magnetic moments of Mo atoms are 1.1 μ_B.

For radioactive Tc, a magnetic Tc(IV) oxide is known. TcO₂ (*mP12*) is isostructural to MoO₂ (*mP12*) with *P2/c* space group (no. 12) and subgroup *P2₁* (no. 4) for the magnetic configuration (identical to VO₂ (*mP12*), Figure 3b) [150]. Overall, very few data on the TcO₂

(*mP12*) are available. We found an antiferromagnetic ground state with magnetic moments of $2.7 \mu_B$ on the metal atoms. Based on our results, TcO_2 (*mP12*) possesses a band gap of 2.4 eV. Compared to the experimental crystal structure, the lattice parameters a , b , and c differ by +1.5%, -3.0% , and 1.0, respectively.

Ru(IV) oxide, RuO_2 (*tP6*), is a rutile structure with space group $P4_2/mnm$ (no. 136) [151]. The symmetry of the magnetically ordered structure is lowered to subgroup $Cmmm$ (no. 65) (identical to VO_2 (*mP12*), Figure 3d). It was originally determined to be paramagnetic within 4–300 K [152], but based on recent experimental and computational work, it is an antiferromagnet with a Neel temperature over 300 K [88]. We found an antiferromagnetic ground state with magnetic moment of $1.5 \mu_B$, whereas the experiments showed small magnetic moments of $0.05 \mu_B$. The lattice parameters of the optimized structure are in good agreement with the experimental data (with differences less than 0.5%).

Rh(IV) oxide, RhO_2 (*tP6*), also adopts the rutile structure with space group $P4_2/mnm$ (no. 136) [153]. We found a ferromagnetic ground state (identical to CrO_2 , Figure 4). Based on our calculations, RhO_2 is metallic (Table 1) [154]. The experimental data on electronic and magnetic properties are limited, and it has only been mentioned that RhO_2 (*tP6*) should be paramagnetic at room temperature [155]. The structural properties are in good agreement with the experimental data: the lattice parameters differ by +0.2% and +0.5% for a and c , respectively.

Ag(II/III) oxide, Ag_3O_4 (*mP14*), crystallizes in a monoclinic crystal structure with space group $P2_1/c$ (no. 14) (Figure 9) [156]. The lattice parameters match the experimental data well: the differences between the optimized and experimental lattice constants are +1.2%, +0.5%, and +0.6% for a , b , and c , respectively. Ag_3O_4 has been reported to be paramagnetic above 70 K [156,157]. At 0 K, we found the ferromagnetic ground state with Ag^{3+} magnetic moments of $0.2 \mu_B$. We found Ag_3O_4 to be the metallic conductor (Table 1). The electronic structure of Ag_3O_4 has been described as magnetic in the literature [158], but no further details on how it was determined or other experimental data were provided.

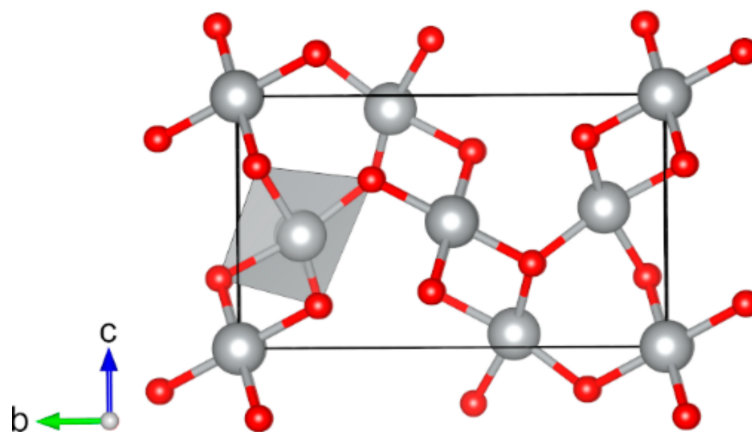


Figure 9. Optimized structure of Ag_3O_4 (*mP14*) (red: O, light grey: Ag). Spins are aligned up along c axis and not visualized. Square planar coordination of Ag atoms is shown in a light-grey color.

2.4. Magnetic Binary 5D-Metal Oxides

W(IV) oxide, WO_2 (*mP12*), has a monoclinic crystal structure with space group $P2_1/c$ (no. 14) [159]. The magnetically ordered structure has a lower symmetry with subgroup $P2_1$ (no. 4) (identical to VO_2 (*mP12*), Figure 3b). To our knowledge, there are no experimental or computational studies on the magnetic properties of WO_2 (*mP12*). The paramagnetic ground state is mentioned in the book by Richards [155], which describes WO_2 as a metallic compound. However, the experimental conditions of the measurements are not provided. Based on our calculations, the ground state of WO_2 (*mP12*) is antiferromagnetic with magnetic moments of $0.4 \mu_B$. The lattice parameters of the calculated structure are in good

agreement with the experimental data, showing differences of -0.2% for a , $+0.6\%$ for b , and $+0.4\%$ for c .

For rhenium, we investigated three Re(IV) magnetic oxides: ReO_2 ($mP12$), ReO_2 ($oP12$), and ReO_2 ($tP6$). ReO_2 ($mP12$) crystallizes in a monoclinic crystal structure with space group $P2_1/c$ (no. 14). For the magnetically ordered structure, the symmetry is lowered to subgroup $P2_1$ (no. 4) (identical to VO_2 ($mP12$) and shown in Figure 3b). Monoclinic ReO_2 ($mP12$) structure is experimentally characterized to be paramagnetic below 573 K [160,161]. ReO_2 ($oP12$) crystallizes in an orthorhombic crystal structure with space group $Pbcn$ (no. 60) [162]. The symmetry of the magnetically ordered structure is lowered to space group $P2_12_12$ (no. 18) (Figure 10). It has been determined to be a metallic and paramagnetic compound between 4.2 K and the room temperature [148]. Based on our calculations at 0 K, ReO_2 ($oP12$) has a band gap of 1.6 eV. We found an antiferromagnetic ground state with magnetic moments of $1.1 \mu_B$. In agreement with our findings, a recent computational study showed that at 0 K, the structure adopts antiferromagnetic ordering [163]. ReO_2 ($tP6$) adopts tetragonal crystal structure with space group $P4_2/mnm$ (no. 136) [162,164,165]. The symmetry of the magnetically ordered structure is lowered to subgroup $Cmmm$ (no. 65) (identical to VO_2 ($tP6$), Figure 3d). The lattice parameters of the optimized ReO_2 ($mP12$) and ReO_2 ($oP12$) structures are in good agreement with experimental data, showing differences of less than 1.1%. However, ReO_2 ($tP6$) shows a difference of about 14% for the lattice constant c . Similar to tetragonal VO_2 , it is possible that tetragonal ReO_2 ($tP6$) structure at 0 K is different from the experimental structure determined at a higher temperature (the material was synthesized at 693 K). Very limited information is available on tetragonal ReO_2 ($tP6$); only one experimental/computational paper has been reported [166]. DFT-LDA + U calculations suggested that the ReO_2 ($tP6$) structure is antiferromagnetic with magnetic moments of $1.0 \mu_B$ on Re atoms. Based on our calculations, the magnetic moment on Re atoms is $2.1 \mu_B$, and the band gap is 1.5 eV.

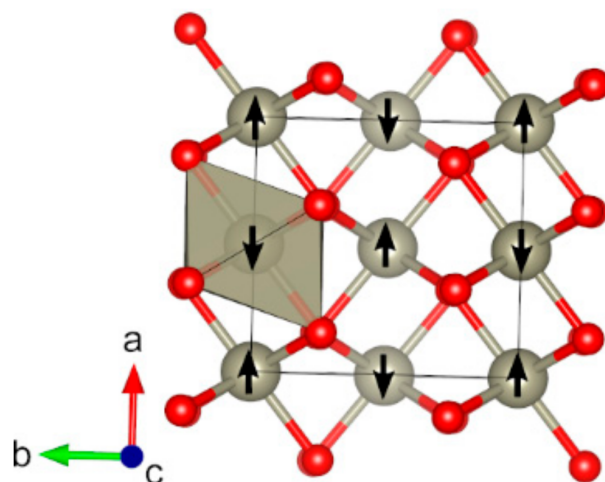


Figure 10. Optimized structure of ReO_2 ($mP12$) (red: O, grey: Re). The directions of magnetic moments are illustrated by black arrows. Coordination octahedra of Re atoms is shown in grey color.

Ir(IV) oxide IrO_2 crystallizes in a tetragonal crystal structure with space group $P4_2/mnm$ (no. 136) [167]. IrO_2 ($tP6$) is considered to be paramagnetic in the temperature range of 4.2–300 K, and we found an antiferromagnetic spin configuration to be energetically the most favorable at 0 K [152]. The magnetic moments are $0.5 \mu_B$. The symmetry of the magnetically ordered structure is lowered to subgroup $Cmmm$ (no. 65), identically to VO_2 ($tP6$) (Figure 3d). The lattice parameters of the calculated structure differ from the experimental data by -0.2% for a , b , and $+0.8\%$ for c . IrO_2 is a metallic conductor [168].

2.5. *d*-Metal Oxides with Molecular Structures

Some binary *d*-metal oxides exist as molecular crystals, where molecular units are held together by weak intermolecular interactions (van der Waals forces): CrO₃ (*oS16*), MoO₃ (*oP16*), WO₃ (*tP8*), Mn₂O₇ (*mP72*), Tc₂O₇ (*oP36*), RuO₄ (*cP40*), RuO₄ (*mS20*), and OsO₄ (*mS20*). Even though the studied molecular crystals are nonmagnetic, they represent interesting cases because the weak intermolecular interactions are not described properly by standard DFT methods such as PBE or PBE0 [169,170]. Table 2 shows a summary of the optimized lattice parameters for the binary *d*-metal oxides with molecular crystal structures.

Table 2. Optimized lattice parameters of binary *d*-metal oxides with molecular crystal structures, obtained at the DFT-PBE0/TZVP and DFT-PBE0-D3/TZVP levels of theory. Errors with respect to experimental lattice parameters are shown in parentheses.

Oxide	Pearson Symbol	Space Group	<i>a</i> (Å)			<i>b</i> (Å)			<i>c</i> (Å)		
			No D3	D3 ZD _a	D3 BJ _b	No D3	D3 ZD	D3 BJ	No D3	D3 ZD	D3 BJ
CrO ₃ [171]	<i>oS16</i>	<i>C2cm</i> (40)	5.748 (0.1%)	5.688 (−1.0%)	5.710 (−0.6%)	8.979 (4.9%)	8.050 (−5.9%)	8.218 (−4.0%)	4.925 (2.8%)	4.715 (−1.6%)	4.711 (−1.6%)
MoO ₃ [172]	<i>oP16</i>	<i>Pbnm</i> (62)	14.477 (4.5%)	13.380 (−3.5%)	13.515 (−2.5%)	3.695 (0%)	3.697 (0%)	3.692 (−0.1%)	3.972 (0.2%)	3.955 (−0.2%)	3.941 (−0.5%)
WO ₃ [173]	<i>tP8</i>	<i>P4/nmm</i> (129)	5.314 (0.2%)	5.294 (−0.2%)	5.297 (−0.1%)				4.020 (2.2%)	4.018 (2.1%)	4.014 (2.0%)
Mn ₂ O ₇ [174]	<i>mP72</i>	<i>P2₁/c</i> (14)	6.986 (2.8%)	6.693 (−1.5%)	6.697 (−1.4%)	17.504 (4.9%)	16.494 (−1.2%)	16.493 (−1.2%)	9.598 (1.5%)	9.023 (−4.6%)	9.063 (−4.1%)
Tc ₂ O ₇ [175]	<i>oP36</i>	<i>Pbca</i> (61)	13.852 (0.7%)	13.543 (−1.5%)	13.535 (−1.6%)	7.600 (2.2%)	6.908 (−7.1%)	7.033 (−5.5%)	5.762 (2.6%)	5.337 (−5.0%)	5.353 (−4.7%)
RuO ₄ [176]	<i>cP40</i>	<i>P-43n</i> (218)	8.761 (3.0%)	8.254 (−3.0%)	8.359 (−1.8%)						
RuO ₄ [176]	<i>mS20</i>	<i>C2/c</i> (15)	9.562 (2.8%)	9.092 (−2.3%)	9.146 (−1.7%)	4.534 (3.1%)	4.231 (−3.8%)	4.318 (−1.8%)	8.673 (2.6%)	8.177 (−3.3%)	8.285 (−2.0%)
OsO ₄ [177]	<i>mS20</i>	<i>C2/c</i> (15)	9.514 (1.4%)	9.066 (−3.3%)	9.058 (−3.4%)	4.572 (1.3%)	4.321 (−4.3%)	4.327 (−4.2%)	8.632 (0%)	8.212 (−4.8%)	8.250 (−4.4%)

^a DFT-D3 with zero-damping scheme [41]. ^b DFT-D3 with Becke–Johnson damping scheme [178].

While DFT-PBE0/TZVP without dispersion correction results in the overestimation of the lattice parameters, the D3 dispersion correction typically significantly underestimates the lattice parameters. For example, the error in lattice constant *b* of Tc₂O₇ −7% for DFT-D3(ZD), compared with +2% without dispersion correction. Most of the studied molecular crystals show ionic bonding, which may be a challenging situation for the DFT-D3 scheme. We also tested the effects of the three-body dispersion term (ABC) on some molecular crystals but found only a negligible effect and no significant improvements.

2.6. Mercury Oxides

Finally, we discuss in more detail some mercury oxides which are rarely mentioned in the literature and have never been carefully studied: α -HgO₂ (*mS6*) with space group *C2/m* (no. 12) and β -HgO₂ (*oP12*) with space group *Pbca* (no. 61) (Figure 11) [179–182]. The crystal structure of α -HgO₂ has been refined assuming a monoclinic symmetry, yielding a distorted CsCl-type structure. Originally, a rhombohedral unit cell with α close to 90° was proposed [181]. β -HgO₂ has been studied more extensively and adopts a distorted version of the cubic MgO₂ structure of group 12 oxides ZnO₂ and CdO₂ [179–181].

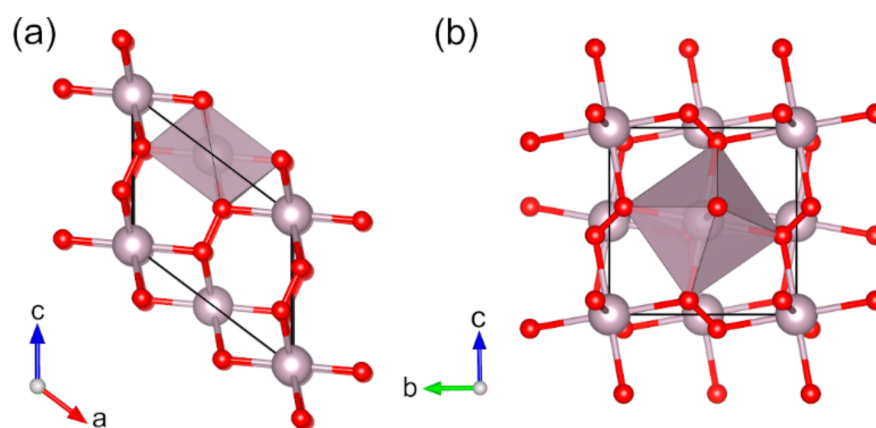


Figure 11. Optimized structures of (a) α -HgO₂ (*mS6*) and (b) β -HgO₂ (*oP12*) (red: oxygen, almond: mercury). Coordination octahedra of Hg atoms are shown in almond color.

Based on our calculations, errors in the lattice parameters a , b , and c , compared with experimental data are +35.9%, −25.5%, and 30.5% for α -HgO₂ (*mS6*) and −10.0%, −8.9%, and +13.8% for β -HgO₂ (*oP12*). Such large errors were not observed for any other d-metal oxide included in the study. The errors are not expected to be due to the DFT-PBE0 method or the used basis set, because the other studied mercury oxides, HgO (*oP8*) and HgO (*hP6*), are described well by DFT-PBE0 (the errors in the lattice parameters are less than 1.3%) (see Supplementary Materials). Our findings motivate further experimental studies on the crystal structures of these oxides. For β -HgO₂, our final optimized geometry corresponds to the cubic MgO₂ structure in space group *Pa-3* (no. 205). No imaginary vibrational frequencies were observed when a harmonic frequency calculation was carried out in this space group.

3. Materials and Methods

All quantum chemical calculations were carried out using the CRYSTAL14 and CRYSTAL17 program packages [40,183]. The structures were fully optimized within the applied space groups by using hybrid PBE0 density functional method (DFT-PBE0, 25% exact exchange) [184,185]. All-electron, Gaussian-type triple- ζ -valence + polarization (TZVP) basis sets based on Karlsruhe def2 basis sets were utilized [186]. Scalar relativistic effects were taken into account by means of relativistic effective core potentials for elements Y–Hg. The molecular basis sets were adapted for solid-state calculations, and all basis sets are given as Supplementary Materials. Furthermore, the results obtained with a smaller split-valence + polarization (SVP) basis set are reported in the Supplementary Materials. For some molecular and layered oxides, where weak intermolecular or interlayer interactions could play a role, Grimme’s D3 dispersion correction scheme was tested both with zero-damping and Becke–Johnson damping [41,178,187]. List of the Monkhorst-Pack-type k -meshes used for sampling the reciprocal space is given in the Supplementary Materials. Spin-unrestricted formalism was used for all magnetic d -metal oxides. Tightened tolerance factors (TOLINTEG) of 8, 8, 8, 8, and 16 were used for the evaluation of the Coulomb and exchange integrals. Default geometry optimization criteria and DFT integration grids of CRYSTAL were used. Harmonic frequency calculations were carried out as implemented in the CRYSTAL software [188,189].

In general, calculations on magnetic oxides were carried out with the following strategy: if experimental data on the magnetic ground state of the crystal structure were available, the reported ground state was calculated. However, there are crystal structures which are only reported as paramagnetic at the room temperature, but the low-temperature magnetic ground state has not been reported. In such cases, we investigated their magnetic and diamagnetic ground states at 0 K, testing various diamagnetic (DM), ferromagnetic (FM), ferrimagnetic (FiM), or antiferromagnetic (AFM) configurations to find the ener-

getically favorable spin configuration (relative energies are given in the Supplementary Materials). We also checked different spin configurations for crystal structures where the magnetic ground state is not known from the experiment. Spin-orbit coupling was not taken into account in the calculations, as spin-orbit coupling is not yet available in the public version of the CRYSTAL code.

All experimental crystal structures were taken from Inorganic Crystal Structure Database (ICSD) [190] or from the Crystallography Open Database (COD) [191,192]. The structures optimized at the DFT-PBE0/TZVP level of theory, including spin configurations for magnetic structures, are available as Supplementary Materials. Structural figures were created using the VESTA software [193].

4. Conclusions

We have carried out a comprehensive and systematic computational study of 100 bulk binary *d*-metal oxides by hybrid DFT-PBE0 method. We reported detailed information on the crystal structures including space groups, spin configurations, band gaps, and atomic magnetic moments, which are consistent with the experimental data. For the first time, we found a few problematic cases such as α - and β -HgO₂ where crystallographic data, considered to be correct for a long time, seem to be inaccurate. We identified the magnetic ground state of the crystal structures at 0 K, which are known to be paramagnetic. Our study shows that hybrid DFT methods represent a reliable methodology for the description of such strongly correlated systems as *d*-metal oxides. The database facilitates future studies on the more complex properties of the binary *d*-metal oxides and provides a dataset for benchmarking new computational methods.

Supplementary Materials: The following supporting information can be downloaded online. Table S1: Summary of the studied binary *d*-metal oxides, Table S2: Lattice parameters of the studied binary *d*-metal oxides, and Table S3: Energy comparisons of different magnetic configurations for the paramagnetic binary *d*-metal oxides. All structural data in CIF format, GTO basis sets used in the calculations.

Author Contributions: Conceptualization, A.J.K.; methodology, M.S.K. and K.E.; investigation, M.S.K., K.E., J.L., A.R. and N.T.; data curation, K.E.; writing—original draft preparation, M.S.K.; writing—review and editing, K.E. and A.J.K.; visualization, M.S.K.; supervision, A.J.K.; funding acquisition, A.J.K. All authors have read and agreed to the published version of the manuscript.

Funding: This research was funded by the Academy of Finland, grant number 317273.

Institutional Review Board Statement: Not applicable.

Informed Consent Statement: Not applicable.

Data Availability Statement: An up-to-date Git repository of the studied *d*-metal oxides is available at <https://github.com/aalto-imm/d-oxides> (accessed on 30 December 2021).

Acknowledgments: The computing resources from CSC, the Finnish IT Center for Science, are gratefully acknowledged.

Conflicts of Interest: The authors declare no conflict of interest.

References

1. Nilius, N. Properties of Oxide Thin Films and Their Adsorption Behavior Studied by Scanning Tunneling Microscopy and Conductance Spectroscopy. *Surf. Sci. Rep.* **2009**, *64*, 595–659. [CrossRef]
2. Giordano, L.; Pachchioni, G. Oxide Films at the Nanoscale: New Structures, New Functions, and New Materials. *Acc. Chem. Res.* **2011**, *44*, 1244–1252. [CrossRef]
3. Honkala, K. Tailoring Oxide Properties: An Impact on Adsorption Characteristics of Molecules and Metals. *Surf. Sci. Rep.* **2014**, *69*, 366–388. [CrossRef]
4. Tripathi, T.S.; Karppinen, M. Atomic Layer Deposition of P-Type Semiconducting Thin Films: A Review. *Adv. Mater. Interfaces* **2017**, *4*, 1–16. [CrossRef]
5. Walia, S.; Balendhran, S.; Nili, H.; Zhuiykov, S.; Rosengarten, G.; Wang, Q.H.; Bhaskaran, M.; Sriram, S.; Strano, M.S.; Kalantar-zadeh, K. Transition Metal Oxides—Thermoelectric Properties. *Prog. Mater. Sci.* **2013**, *58*, 1443–1489. [CrossRef]

6. Rao, C.N.R. Transition Metal Oxides. *Annu. Rev. Phys. Chem.* **1989**, *40*, 291–326. [[CrossRef](#)]
7. Dixon, S.C.; Scanlon, D.O.; Carmalt, C.J.; Parkin, I.P. N-Type Doped Transparent Conducting Binary Oxides: An Overview. *J. Mater. Chem. C* **2016**, *4*, 6946–6961. [[CrossRef](#)]
8. Wang, L.; Maxisch, T.; Ceder, G. Oxidation Energies of Transition Metal Oxides within the GGA+U Framework. *Phys. Rev. B* **2006**, *73*, 195107. [[CrossRef](#)]
9. Schrön, A.; Rödl, C.; Bechstedt, F. Crystalline and Magnetic Anisotropy of the 3d-Transition Metal Monoxides MnO, FeO, CoO, and NiO. *Phys. Rev. B* **2012**, *86*, 115134. [[CrossRef](#)]
10. Noh, J.; Osman, O.I.; Aziz, S.G.; Winget, P.; Brédas, J.L. A Density Functional Theory Investigation of the Electronic Structure and Spin Moments of Magnetite. *Sci. Technol. Adv. Mater.* **2014**, *15*, 044202. [[CrossRef](#)]
11. Lima, A.F. Density Functional Theory Study on the Magnetic Properties of Co₃O₄ with Normal Spinel Structure. *J. Phys. Chem. Solids* **2016**, *91*, 86–89. [[CrossRef](#)]
12. Singh, V.; Kosa, M.; Majhi, K.; Major, D.T. Putting DFT to the Test: A First-Principles Study of Electronic, Magnetic, and Optical Properties of Co₃O₄. *J. Chem. Theory Comput.* **2015**, *11*, 64–72. [[CrossRef](#)] [[PubMed](#)]
13. Deng, H.X.; Li, J.; Li, S.S.; Xia, J.B.; Walsh, A.; Wei, S.H. Origin of Antiferromagnetism in CoO: A Density Functional Theory Study. *Appl. Phys. Lett.* **2010**, *96*, 162508. [[CrossRef](#)]
14. Bredow, T.; Gerson, A.R. Effect of Exchange and Correlation on Bulk Properties of MgO, NiO, and CoO. *Phys. Rev. B* **2000**, *61*, 5194–5201. [[CrossRef](#)]
15. Rollmann, G.; Rohrbach, A.; Entel, P.; Hafner, J. First-Principles Calculation of the Structure and Magnetic Phases of Hematite. *Phys. Rev. B* **2004**, *69*, 165107. [[CrossRef](#)]
16. Linnera, J.; Karttunen, A.J. Ab Initio Study of the Lattice Thermal Conductivity of Cu₂O Using the Generalized Gradient Approximation and Hybrid Density Functional Methods. *Phys. Rev. B* **2017**, *96*, 014304. [[CrossRef](#)]
17. Rödl, C.; Fuchs, F.; Furthmüller, J.; Bechstedt, F. Quasiparticle Band Structures of the Antiferromagnetic Transition-Metal Oxides MnO, FeO, CoO, and NiO. *Phys. Rev. B* **2009**, *79*, 235114. [[CrossRef](#)]
18. Kulik, H.J.; Marzari, N. Transition-Metal Dioxides: A Case for the Intersite Term in Hubbard-Model Functionals. *J. Chem. Phys.* **2011**, *134*, 094103. [[CrossRef](#)]
19. Chen, X.; Parker, D.; Du, M.H.; Singh, D.J. Potential Thermoelectric Performance of Hole-Doped Cu₂O. *New J. Phys.* **2013**, *15*, 043029. [[CrossRef](#)]
20. Seo, D.H.; Urban, A.; Ceder, G. Calibrating Transition-Metal Energy Levels and Oxygen Bands in First-Principles Calculations: Accurate Prediction of Redox Potentials and Charge Transfer in Lithium Transition-Metal Oxides. *Phys. Rev. B* **2015**, *92*, 115118. [[CrossRef](#)]
21. Kirchner-Hall, N.E.; Zhao, W.; Xiong, Y.; Timrov, I.; Dabo, I. Extensive Benchmarking of DFT+U Calculations for Predicting Band Gaps. *Appl. Sci.* **2021**, *11*, 2395. [[CrossRef](#)]
22. Gillen, R.; Robertson, J. Accurate Screened Exchange Band Structures for the Transition Metal Monoxides MnO, FeO, CoO and NiO. *J. Phys. Condens. Matter* **2013**, *25*, 165502. [[CrossRef](#)] [[PubMed](#)]
23. Zhao, Q.; Kulik, H.J. Where Does the Density Localize in the Solid State? Divergent Behavior for Hybrids and DFT+U. *J. Chem. Theory Comput.* **2018**, *14*, 670–683. [[CrossRef](#)] [[PubMed](#)]
24. Sun, J.; Ruzsinszky, A.; Perdew, J. Strongly Constrained and Appropriately Normed Semilocal Density Functional. *Phys. Rev. Lett.* **2015**, *115*, 1–6. [[CrossRef](#)] [[PubMed](#)]
25. Lane, C.; Furness, J.W.; Buda, I.G.; Zhang, Y.; Markiewicz, R.S.; Barbiellini, B.; Sun, J.; Bansil, A. Antiferromagnetic Ground State of La₂CuO₄: A Parameter-Free Ab Initio Description. *Phys. Rev. B* **2018**, *98*, 125140. [[CrossRef](#)]
26. Kylänpää, L.; Balachandran, J.; Ganesh, P.; Heinonen, O.; Kent, P.R.C.; Krogel, J.T. Accuracy of Ab Initio Electron Correlation and Electron Densities in Vanadium Dioxide. *Phys. Rev. Mater.* **2017**, *1*, 065408. [[CrossRef](#)]
27. Tran, F.; Stelzl, J.; Blaha, P. Rungs 1 to 4 of DFT Jacob’s Ladder: Extensive Test on the Lattice Constant, Bulk Modulus, and Cohesive Energy of Solids. *J. Chem. Phys.* **2016**, *144*. [[CrossRef](#)]
28. Isaacs, E.B.; Wolverton, C. Performance of the Strongly Constrained and Appropriately Normed Density Functional for Solid-State Materials. *Phys. Rev. Mater.* **2018**, *2*, 063801. [[CrossRef](#)]
29. Charles, N.; Rondinelli, J.M. Assessing Exchange-Correlation Functional Performance for Structure and Property Predictions of Oxyfluoride Compounds from First Principles. *Phys. Rev. B* **2016**, *94*. [[CrossRef](#)]
30. Kuklin, M.S.; Karttunen, A.J. Crystal Structure Prediction of Magnetic Transition Metal Oxides by Using Evolutionary Algorithm and Hybrid DFT Methods. *J. Phys. Chem. C* **2018**, *122*, 24949–24957. [[CrossRef](#)]
31. Brugnoli, L.; Ferrari, A.M.; Civalleri, B.; Pedone, A.; Menziani, M.C. Assessment of Density Functional Approximations for Highly Correlated Oxides: The Case of CeO₂ and Ce₂O₃. *J. Chem. Theory Comput.* **2018**, *14*, 4914–4927. [[CrossRef](#)] [[PubMed](#)]
32. Civalleri, B.; Presti, D.; Dovesi, R.; Savin, A. On Choosing the Best Density Functional Approximation. In *Chemical Modelling*; Springborg, M., Ed.; Royal Society of Chemistry: Cambridge, UK, 2012; Volume 9, pp. 168–185. ISBN 978-1-84973-412-7.
33. Moreira, I.d.P.R.; Illas, F.; Martin, R.L. Effect of Fock Exchange on the Electronic Structure and Magnetic Coupling in NiO. *Phys. Rev. B Condens. Matter Mater. Phys.* **2002**, *65*, 1551021. [[CrossRef](#)]
34. Linnera, J.; Sansone, G.; Maschio, L.; Karttunen, A.J. Thermoelectric Properties of P-Type Cu₂O, CuO, and NiO from Hybrid Density Functional Theory. *J. Phys. Chem. C* **2018**, *122*, 15180–18189. [[CrossRef](#)] [[PubMed](#)]

35. Das, T.; Liberto, D.G.; Tosoni, S.; Pacchioni, G. Band Gap of 3d Metal Oxides and Quasi-2D Materials from Hybrid Density Functional Theory: Are Dielectric-Dependent Functionals Superior? *J. Chem. Theory Comput.* **2019**, *16*, 3786–3798. [[CrossRef](#)] [[PubMed](#)]
36. Cipriano, L.A.; Liberto, D.G.; Tosoni, S.; Pacchioni, G. Band Gap in Magnetic Insulators from a Charge Transition Level Approach. *J. Chem. Theory Comput.* **2019**, *15*, 6294–6312. [[CrossRef](#)] [[PubMed](#)]
37. Li, W.; Walther, C.F.J.; Kuc, A.; Heine, T. Density Functional Theory and Beyond for Band-Gap Screening: Performance for Transition-Metal Oxides and Dichalcogenides. *J. Chem. Theory Comput.* **2013**, *9*, 2950–2958. [[CrossRef](#)] [[PubMed](#)]
38. Posysaev, S.; Miroshnichenko, O.; Alatalo, M.; Le, D.; Rahman, T.S. Oxidation States of Binary Oxides from Data Analytics of the Electronic Structure. *Comput. Mater. Sci.* **2019**, *161*, 403–414. [[CrossRef](#)]
39. Dovesi, R.; Erba, A.; Orlando, R.; Zicovich-Wilson, C.M.; Civalieri, B.; Maschio, L.; Rérat, M.; Casassa, S.; Baima, J.; Salustro, S.; et al. Quantum-Mechanical Condensed Matter Simulations with CRYSTAL. *Wiley Interdiscip. Rev. Comput. Mol. Sci.* **2018**, *8*, 1–36. [[CrossRef](#)]
40. Grimme, S.; Antony, J.; Ehrlich, S.; Krieg, H. A Consistent and Accurate Ab Initio Parametrization of Density Functional Dispersion Correction (DFT-D) for the 94 Elements H-Pu. *J. Chem. Phys.* **2010**, *132*, 154104. [[CrossRef](#)]
41. Honig, J.M.; Reed, T.B. Electrical Properties of Ti₂O₃ Single Crystals. *Phys. Rev.* **1968**, *174*, 1020–1026. [[CrossRef](#)]
42. Ohkoshi, S.; Tsunobuchi, Y.; Matsuda, T.; Hashimoto, K.; Namai, A.; Hakoe, F.; Tokoro, H. Synthesis of a Metal Oxide with a Room-Temperature Photoreversible Phase Transition. *Nat. Chem.* **2010**, *2*, 539–545. [[CrossRef](#)] [[PubMed](#)]
43. Tanaka, K.; Nasu, T.; Miyamoto, Y.; Ozaki, N.; Tanaka, S.; Nagata, T.; Hakoe, F.; Yoshikiyo, M.; Nakagawa, K.; Umeta, Y.; et al. Structural Phase Transition between Lambda-Ti₃O₅ and Delta-Ti₃O₅ by Breaking of a One-Dimensionally Conducting Pathway. *Cryst. Growth Des.* **2015**, *15*, 653–657. [[CrossRef](#)]
44. Moon, R.M. Antiferromagnetism in V₂O₃. *Phys. Rev. Lett.* **1970**, *25*, 527–529. [[CrossRef](#)]
45. Thomas, G.A.; Rapkine, D.H.; Carter, S.A.; Millis, A.J. Observation of the Gap and Kinetic Energy in a Correlated Insulator. *Phys. Rev. Lett.* **1994**, *73*, 1529–1532. [[CrossRef](#)]
46. Berglund, C.N.; Guggenheim, H.J. Electronic Properties of VO₂ near the Semiconductor-Metal Transition. *Phys. Rev.* **1969**, *185*, 1022–1033. [[CrossRef](#)]
47. Hill, A.H.; Harrison, A.; Dickinson, C.; Zhou, W.; Kockelmann, W. Crystallographic and Magnetic Studies of Mesoporous Eskolaite, Cr₂O₃. *Microporous Mesoporous Mater.* **2010**, *130*, 280–286. [[CrossRef](#)]
48. Crawford, J.A.; Vest, R.W. Electrical Conductivity of Single-Crystal Cr₂O₃. *J. Appl. Phys.* **1964**, *35*, 2413–2418. [[CrossRef](#)]
49. Cheng, C.-S.; Gomi, H.; Sakata, H. Electrical and Optical Properties of Cr₂O₃ Films Prepared by Chemical Vapour Deposition. *Phys. Stat. Sol.* **1996**, *155*, 417–425. [[CrossRef](#)]
50. Kubota, B. Preparation of Ferromagnetic Chromium Dioxide. *J. Phys. Soc. Jpn.* **1960**, *15*, 1706. [[CrossRef](#)]
51. Cheetham, A.K.; Hope, D.A.O. Magnetic Ordering and Exchange Effects in the Antiferromagnetic Solid Solutions Mn_xNi_{1-x}O. *Phys. Rev. B* **1983**, *27*, 6964–6967. [[CrossRef](#)]
52. Drabkin, I.A.; Emel'yanova, L.T.; Iskenderov, R.N.; Ksendzov, Y.M. Photoconductivity of Single Crystals of MnO. *Sov. Phys. Solid State* **1969**, *10*, 2428.
53. Iskenderov, R.N.; Drabkin, I.A.; Evel'yanova, L.T.; Ksendzov, Y.M. Absorption Spectrum of MnO Single Crystals. *Sov. Phys. Solid State* **1969**, *10*, 2031.
54. Cockayne, E.; Levin, I.; Wu, H.; Llobet, A. The Magnetic Structure of Bixbyite α -Mn₂O₃: A Combined Density Functional Theory DFT+U and Neutron Diffraction Study. *Phys. Rev. B* **2012**, *87*, 184413. [[CrossRef](#)]
55. Regulski, M.; Przeniosło, R.; Sosnowska, I.; Hohlwein, D.; Schneider, R. Neutron Diffraction Study of the Magnetic Structure of α -Mn₂O₃. *J. Alloys Compd.* **2004**, *362*, 236–240. [[CrossRef](#)]
56. Sharma, S.; Chauhan, P.; Husain, S. Structural and Optical Properties of Mn₂O₃ Nanoparticles & Its Gas Sensing Applications. *Adv. Mater. Proc.* **2016**, *2*, 220–225. [[CrossRef](#)]
57. Awad, H.D.; Elttayef, A.K.; Ressen, A.L.; Ali, K.A. The Effect of Annealing on the Structural and Optical Properties of Mn₂O₃ Thin Film Prepared by Chemical Spray Pyrolysis. *Int. J. Sci. Res.* **2017**, *6*, 291–294. [[CrossRef](#)]
58. Bose, V.C.; Maniammal, K.; Madhu, G.; Veenas, C.L.; Aiswarya, R.; Biju, V. DC Electrical Conductivity of Nanocrystalline Mn₃O₄ Synthesized through a Novel Sol-Gel Route. *Int. Conf. Mater. Sci. Technol.* **2015**, *73*, 012084. [[CrossRef](#)]
59. Gao, T.; Glerup, M.; Krumeich, F.; Nesper, R.; Fjellvåg, H.; Norby, P. Microstructures and Spectroscopic Properties of Cryptomelane-Type Manganese Dioxide Nanofibers. *J. Phys. Chem. C* **2008**, *112*, 13134–13140. [[CrossRef](#)]
60. Li, T.; Wu, J.; Xiao, X.; Zhang, B.; Hu, Z.; Zhou, J. Band Gap Engineering of MnO₂ through in Situ Al-Doping for Applicable Pseudocapacitors. *RCS Adv.* **2016**, *6*, 13914–13919. [[CrossRef](#)]
61. Druilhe, R.; Suchet, J.P. Electron Transport in CrO₂ and Mn_xCr_{1-x}O₂. *Czech. J. Phys. B* **1967**, *17*, 337–346. [[CrossRef](#)]
62. Greedan, J.E.; Raju, N.P.; Wills, A.S.; Morin, C.; Shaw, S.M.; Reimers, J.N. Structure and Magnetism in λ -MnO₂. Geometric Frustration in a Defect Spinel. *Chem. Mater.* **1998**, *10*, 3058–3067. [[CrossRef](#)]
63. Bhargande, S.K.; Patil, P.S. Structural, Optical Investigation of Manganese Oxide Thin Films by Spray Pyrolysis Technique. *Res. Rev. J. Pure Appl. Phys. Struct* **2013**, *1*, 19–23.
64. Rakhecha, V.C.; Murthy, N.S.S. Spin-Transfer Due to Covalency for the Tetrahedral-Site Fe³⁺ Ions in Fe₃O₄. *J. Phys. C Solid State Phys.* **1978**, *11*, 4389–4404. [[CrossRef](#)]

65. Wright, J.P.; Attfield, J.P.; Radaelli, P.G. Charge Ordered Structure of Magnetite Fe_3O_4 below the Verwey Transition. *Phys. Rev. B* **2002**, *66*, 214422. [[CrossRef](#)]
66. Krén, E.; Szabó, P.; Konczos, G. Neutron Diffraction Studies on the $(1-x)\text{Fe}_2\text{O}_3-x\text{Rh}_2\text{O}_3$ System. *Phys. Lett.* **1965**, *19*, 103–104. [[CrossRef](#)]
67. Maslen, E.N.; Streltsov, V.A.; Streltsova, N.R.; Ishizawa, N. Synchrotron X-Ray Study of the Electron Density in $\alpha\text{-Fe}_2\text{O}_3$. *Acta Crystallogr. Sect. B Struct. Sci.* **1994**, *50*, 435–441. [[CrossRef](#)]
68. Finger, L.W.; Hazen, R.M. Crystal Structure and Isothermal Compression of Fe_2O_3 , Cr_2O_3 , and V_2O_3 to 50 kbars. *J. Appl. Phys.* **1980**, *51*, 5362–5367. [[CrossRef](#)]
69. Malina, O.; Tuček, J.; Jakubec, P.; Kašík, J.; Medřík, I.; Tokoro, H.; Yoshikiyo, M.; Namai, A.; Ohkoshi, S.; Zbořil, R. Magnetic Ground State of Nanosized $\beta\text{-Fe}_2\text{O}_3$ and Its Remarkable Electronic Features. *RSC Adv.* **2015**, *5*, 49719–49727. [[CrossRef](#)]
70. Yoshikiyo, M.; Yamada, K.; Namai, A.; Ohkoshi, S.-I. Study of the Electronic Structure and Magnetic Properties of $\varepsilon\text{-Fe}_2\text{O}_3$ by First-Principles Calculation and Molecular Orbital Calculations. *J. Phys. Chem. C* **2012**, *116*, 8688–8691. [[CrossRef](#)]
71. Khan, D.C.; Erickson, R.A. Magnetic Form Factor of Co^{++} Ion in Cobaltous Oxide. *Phys. Rev. B* **1970**, *1*, 2243–2249. [[CrossRef](#)]
72. Herrmann-Ronzaud, D.; Burlet, P.; Rossat-Mignod, J. Equivalent Type-II Magnetic Structures: CoO , a Collinear Antiferromagnet. *J. Phys. C Solid State Phys.* **1978**, *11*, 2123–2137. [[CrossRef](#)]
73. Sasaki, S.; Fujino, K.; Takéuchi, Y. X-Ray Determination of Electron-Density Distributions in Oxides, MgO , MnO , CoO , and NiO , and Atomic Scattering Factors of Their Constituent Atoms. *Proc. Jpn. Acad. Ser. B Phys. Biol. Sci.* **1979**, *55*, 43–48. [[CrossRef](#)]
74. Ikeda, Y.; Sugiyama, J.; Nozaki, H.; Itahara, H.; Brewer, J.H.; Ansaldo, E.J.; Morris, G.D.; Andreica, D.; Amato, A. Spatial Inhomogeneity of Magnetic Moments in the Cobalt Oxide Spinel Co_3O_4 . *Phys. Rev. B Condens. Matter Mater. Phys.* **2007**, *75*, 1–8. [[CrossRef](#)]
75. Roth, W.L. The Magnetic Structure of Co_3O_4 . *J. Phys. Chem. Solids* **1964**, *25*, 1–10. [[CrossRef](#)]
76. Qiao, L.; Xiao, H.Y.; Meyer, H.M.; Sun, J.N.; Rouleau, C.M.; Puzos, A.A.; Geohegan, D.B.; Ivanov, I.N.; Yoon, M.; Weber, W.J.; et al. Nature of the Band Gap and Origin of the Electro-/Photo-Activity of Co_3O_4 . *J. Mater. Chem. C* **2013**, *1*, 4628–4633. [[CrossRef](#)]
77. Alperin, H.A. The Magnetic Form Factor of Nickel Oxide. *J. Phys. Soc. Jpn. Suppl. B.* **1962**, *17*, 12–15.
78. Fender, B.E.F.; Jacobson, A.J.; Wedgwood, F.A. Covalency Parameters in MnO , $\alpha\text{-MnS}$, and NiO . *J. Chem. Phys.* **1968**, *48*, 990–994. [[CrossRef](#)]
79. Hüfner, S.; Osterwalder, J.; Riesterer, T.; Hulliger, F. Photoemission and Inverse Photoemission Spectroscopy of NiO . *Solid State Commun.* **1984**, *52*, 793–796. [[CrossRef](#)]
80. Sawatzky, G.A.; Allen, J.W. Magnitude and Origin of the Band Gap in NiO . *Phys. Rev. Lett.* **1984**, *53*, 2339–2342. [[CrossRef](#)]
81. Forsyth, J.B.; Brown, P.J.; Wanklyn, B.M. Magnetism in Cupric Oxide. *J. Phys. C Solid State Phys.* **1988**, *21*, 2917–2929. [[CrossRef](#)]
82. Yang, B.X.; Thurston, T.R.; Tranquada, J.M.; Shirane, G. Magnetic Neutron Scattering Study of Single-Crystal Cupric Oxide. *Phys. Rev. B* **1989**, *39*, 4343–4349. [[CrossRef](#)] [[PubMed](#)]
83. Yang, B.; Tranquada, J.; Shirane, G. Neutron Scattering Studies of the Magnetic Structure of Cupric Oxide. *Phys. Rev. B Condens. Matter Mater. Phys.* **1988**, *38*, 174–178. [[CrossRef](#)] [[PubMed](#)]
84. Marabelli, F.; Parravicini, G.B.; Salghetti-Drioli, F. Optical Gap of CuO . *Phys. Rev. B* **1995**, *52*, 1433–1436. [[CrossRef](#)] [[PubMed](#)]
85. Pinsard-Gaudart, L.; Rodriguez-Carvajal, J.; Gukasov, A.; Monod, P. Magnetic Properties of Paramelaconite (Cu_4O_3): A Pyrochlore Lattice with $S=1/2$. *Phys. Rev. B* **2004**, *69*, 104408. [[CrossRef](#)]
86. Meyer, B.K.; Polity, A.; Reppin, D.; Becker, M.; Hering, P.; Klar, P.J.; Sander, T.; Reindl, C.; Benz, J.; Eickhoff, M.; et al. Binary Copper Oxide Semiconductors: From Materials towards Devices. *Phys. Status Solidi B* **2012**, *249*, 1487–1509. [[CrossRef](#)]
87. Berlijn, T.; Snijders, P.C.; Delaire, O.; Zhou, H.; Maier, T.A.; Cao, H.; Chi, S.; Matsuda, M.; Wang, Y.; Koehler, M.R.; et al. Itinerant Antiferromagnetism in RuO_2 . *Phys. Rev. Lett.* **2017**, *118*, 077201. [[CrossRef](#)]
88. Rice, C.E.; Robinson, W.R. Structural Changes Associated with the Semiconductor-to-Metal Transition in Ti_2O_3 . *Mater. Res. Bull.* **1976**, *11*, 1355–1359. [[CrossRef](#)]
89. Guo, Y.; Clark, S.J.; Robertson, J. Electronic and Magnetic Properties of Ti_2O_3 , Cr_2O_3 , and Fe_2O_3 Calculated by the Screened Exchange Hybrid Density Functional. *J. Phys. Condens. Matter* **2012**, *24*, 325504. [[CrossRef](#)]
90. Onoda, M. Phase Transitions of Ti_3O_5 . *J. Solid State Chem.* **1998**, *136*, 67–73. [[CrossRef](#)]
91. Steiner, H.; Turrillasb, X.; Steele, B.C.H. Phase Relationships and Electrical Properties of Ti_3O_5 , CrTi_2O_5 and the Pseudobrookite-Type Systems $\text{Mg}_x\text{Ti}_{3-x}\text{O}_5$ and $\text{Li}_x\text{Ti}_{3-x}\text{O}_5$. *J. Mater. Chem.* **1992**, *2*, 1249–1256. [[CrossRef](#)]
92. Åsbrink, S.; Magnéli, A. Crystal Structure Studies on Triticium Pentoxide, Ti_3O_5 . *Acta Crystallogr.* **1959**, *12*, 575–581. [[CrossRef](#)]
93. Hong, B.Y.S.; Åsbrink, S. The Structure of Gamma- Ti_3O_5 at 297 K. *Acta Cryst.* **1982**, 2570–2576. [[CrossRef](#)]
94. Dernier, P.D.; Marezio, M. Crystal Structure of the Low-Temperature Antiferromagnetic Phase of V_2O_3 . *Phys. Rev. B* **1970**, *2*, 3771–3776. [[CrossRef](#)]
95. Dernier, P.D. The Crystal Structure of V_2O_3 and $(\text{V}_{0.962}\text{Cr}_{0.0382})_2\text{O}_3$ near the Metal-Insulator Transition. *J. Phys. Chem. Solids* **1970**, *31*, 2569–2575. [[CrossRef](#)]
96. Catti, M.; Sandrone, G.; Dovesi, R. Periodic Unrestricted Hartree-Fock Study of Corundum like Ti_2O_3 and V_2O_3 . *Phys. Rev. B Condens. Matter Mater. Phys.* **1997**, *55*, 16122–16131. [[CrossRef](#)]
97. Qazilbash, M.M.; Schafgans, A.A.; Burch, K.S.; Yun, S.J.; Chae, B.G.; Kim, B.J.; Kim, H.T.; Basov, D.N. Electrodynamics of the Vanadium Oxides VO_2 and V_2O_3 . *Phys. Rev. B Condens. Matter Mater. Phys.* **2008**, *77*, 1–10. [[CrossRef](#)]

98. Rogers, K.D. An X-ray Diffraction Study of Semiconductor and Metallic Vanadium Dioxide. *Powder Diffraction*. **1993**, *8*, 240–244. [[CrossRef](#)]
99. Théobald, F.; Cabala, R.; Bernard, J. Essai Sur La Structure de VO₂(B). *J. Solid State Chem.* **1976**, *17*, 431–438. [[CrossRef](#)]
100. Kung, H.H. *Transition Metal Oxides: Surface Chemistry and Catalysis*; Elsevier: Amsterdam, The Netherlands, 1989.
101. Pintchovski, F.; Glaunsinger, W.S.; Navrotsky, A. Experimental Study of the Electronic and Lattice Contributions to the VO₂ Transition. *J. Phys. Chem. Solids* **1978**, *39*, 941–949. [[CrossRef](#)]
102. Park, J.H.; Coy, J.M.; Serkan Kasirga, T.; Huang, C.; Fei, Z.; Hunter, S.; Cobden, D.H. Measurement of a Solid-State Triple Point at the Metal-Insulator Transition in VO₂. *Nature* **2013**, *500*, 431–434. [[CrossRef](#)]
103. Grau-Crespo, R.; Wang, H.; Schwingenschlög, U. Why the Heyd-Scuseria-Ernzerhof Hybrid Functional Description of VO₂ Phases Is Not Correct. *Phys. Rev. B Condens. Matter Mater. Phys.* **2012**, *86*, 2–5. [[CrossRef](#)]
104. Burdett, J.K.; Miller, G.J.; Richardson, J.W.; Smith, V.J. Low-Temperature Neutron Powder Diffraction Study of Chromium Dioxide and the Validity of the Jahn-Teller Viewpoint. *J. Am. Chem. Soc.* **1988**, *110*, 8064–8071. [[CrossRef](#)]
105. Tan, M.; Tao, X. Ab Initio Electronic Structure of CrO₂. *Chin. Phys. Lett.* **1999**, *16*, 199–201. [[CrossRef](#)]
106. Li, X.W.; Gupta, A.; Xiao, G. Influence of Strain on the Magnetic Properties of Epitaxial (100) Chromium Dioxide (CrO₂) Films. *Appl. Phys. Lett.* **1999**, *75*, 713–715. [[CrossRef](#)]
107. Yang, F.Y.; Chien, C.L.; Li, X.W.; Xiao, G.; Gupta, A. Critical Behavior of Epitaxial Half-Metallic Ferromagnetic CrO₂ films. *Phys. Rev. B Condens. Matter Mater. Phys.* **2001**, *63*, 2–5. [[CrossRef](#)]
108. Blech, I.A.; Averbach, B.L. Spin Correlations in MnO. *Physics* **1964**, *1*, 31–44. [[CrossRef](#)]
109. Nam, K.M.; Kim, I.Y.; Jo, Y.; Lee, S.M.; Kim, B.G.; Choi, R.; Choi, I.S.; Song, H.; Park, J.T. New Crystal Structure: Synthesis and Characterization of Hexagonal Wurtzite MnO. *J. Am. Chem. Soc.* **2012**, *134*, 8392–8395. [[CrossRef](#)]
110. Schrön, A.; Rödl, C.; Bechstedt, F. Energetic Stability and Magnetic Properties of MnO in the Rocksalt, Wurtzite, and Zinc-Blende Structures: Influence of Exchange and Correlation. *Phys. Rev. B Condens. Matter Mater. Phys.* **2010**, *82*, 165109. [[CrossRef](#)]
111. Geller, S. Structure of Alpha-Mn₂O₃, (Mn_{0.983}Fe_{0.017})₂O₃ and (Mn_{0.37}Fe_{0.63})₂O₃ and Relation to Magnetic Ordering. *Acta Crystallogr. Sect. B Struct. Crystallogr. Cryst. Chem.* **1971**, *27*, 821–828. [[CrossRef](#)]
112. Norrestam, R. Alpha-Manganese (III) Oxide—a C-Type Sesquioxide of Orthorhombic Symmetry. *Acta Chem. Scand.* **1967**, *21*, 2871–2884. [[CrossRef](#)]
113. Chevalier, R.R.; Roult, G.; Bertaut, E.F. Etude Par Effet Mossbauer Du Systeme Mn_{2-x}Fe_xO₃-et Transitions Magnetiques Dans Mn₂O₃ Par Diffraction Neutronique. *Solid State Commun.* **1967**, *5*, 7–11. [[CrossRef](#)]
114. Sharrouf, M.; Awad, R.; Roumié, M.; Marhaba, S. Structural, Optical and Room Temperature Magnetic Study of Mn₂O₃ Nanoparticles. *Mater. Sci. Appl.* **2015**, 850–859. [[CrossRef](#)]
115. Satomi, K. Oxygen Positional Parameters of Tetragonal Mn₃O₄. *J. Phys. Soc. Jpn.* **1961**, *16*, 258–266. [[CrossRef](#)]
116. Paris, E.; Ross, I.; Charles, R.; Olijnyk, H. Mn₃O₄ at High Pressure: A Diamond-Anvil Cell Study and a Structural Modelling. *Eur. J. Mineral.* **1992**, *4*, 87–94. [[CrossRef](#)]
117. Franchini, C.; Podloucky, R.; Paier, J.; Marsman, M.; Kresse, G. Ground-State Properties of Multivalent Manganese Oxides: Density Functional and Hybrid Density Functional Calculations. *Phys. Rev. B Condens. Matter Mater. Phys.* **2007**, *75*, 195128. [[CrossRef](#)]
118. Chartier, A.; Arco, P.D.; Dovesi, R.; Giuria, P.; Torino, I.; Saunders, V.R. Ab Initio Hartree-Fock Investigation of the Structural, Electronic, and Magnetic Properties of Mn₃O₄. *Phys. Rev. B* **1999**, *60*, 42–48. [[CrossRef](#)]
119. Rossouw, M.H.; Liles, D.C.; Thackeray, M.M. Alpha Manganese Dioxide for Lithium Batteries: A Structural and Electrochemical Study. *Mat. Res. Bull.* **1992**, *27*, 221–230. [[CrossRef](#)]
120. Fong, C.; Kennedy, B.J.; Elcombe, M.M. A Powder Neutron Diffraction Study of Lambda and Gamma Manganese Dioxide and of LiMn₂O₄. *Z. Krist.* **1994**, *209*, 941–945. [[CrossRef](#)]
121. Bolzan, A.A.; Fong, C.; Kennedy, B.J.; Howard, C.J. Powder Neutron Diffraction Study of Pyrolusite, Beta-MnO₂. *Aust. J. Chem.* **1993**, *46*, 939–944. [[CrossRef](#)]
122. Vadlamani, B.; An, K.; Jagannathan, M.; Chandran, K.S.R. An In-Situ Electrochemical Cell for Neutron Diffraction Studies of Phase Transitions in Small Volume Electrodes of Li-Ion Batteries. *J. Electrochem. Soc.* **2014**, *161*, A1731–A1741. [[CrossRef](#)]
123. Yoshimori, A. A New Type of Antiferromagnetic Structure in the Rutile Type Crystal. *J. Phys. Soc. Jpn.* **1959**, *14*, 807–821. [[CrossRef](#)]
124. Sato, H.; Wakiya, K.; Enoki, T.; Kiyama, T.; Wakabayashi, Y.; Nakao, H.; Murakami, Y. Magnetic Structure of β-MnO₂: X-Ray Magnetic Scattering Study. *J. Phys. Soc. Jpn.* **2001**, *70*, 37–40. [[CrossRef](#)]
125. Yamamoto, N.; Endo, T.; Shimada, M.; Takada, T. Single Crystal Growth of Alpha-MnO₂. *Jpn. J. Appl. Phys.* **1974**, *13*, 723–724. [[CrossRef](#)]
126. Guo, L.W.; Peng, D.L.; Makino, H.; Hanada, T.; Hong, S.K.; Sumiyama, K.; Yao, T.; Inaba, K. Structural Characteristics and Magnetic Properties of λ-MnO₂ Films Grown by Plasma-Assisted Molecular Beam Epitaxy. *J. Appl. Phys.* **2001**, *90*, 351–354. [[CrossRef](#)]
127. Mazzocchi, V.L.; Parente, C.B.R. Refinement of the Ferri- and Paramagnetic Phases of Magnetite from Neutron Multiple Diffraction Data. *J. Appl. Crystallogr.* **1998**, *31*, 718–725. [[CrossRef](#)]
128. Cornell, R.M.; Schwertmann, U. *The Iron Oxides: Structure, Properties, Reactions, Occurrences, and Uses*; Wiley: Weinheim, Germany, 2003; ISBN 978-3-527-60644-3.

129. Masrour, R.; Hlil, E.K.; Hamedoun, M.; Benyoussef, A.; Mounkachi, O.; El Moussaoui, H. Electronic and Magnetic Structures of Fe₃O₄ ferrimagnetic Investigated by First Principle, Mean Field and Series Expansions Calculations. *J. Magn. Magn. Mater.* **2015**, *378*, 37–40. [[CrossRef](#)]
130. Danno, T.; Nakatsuka, D.; Kusano, Y.; Asaoka, H.; Nakanishi, M.; Fujii, T.; Ikeda, Y.; Takada, J. Crystal Structure of β -Fe₂O₃ and Topotactic Phase Transformation to α -Fe₂O₃. *Cryst. Growth Des.* **2013**, *13*, 770–774. [[CrossRef](#)]
131. Kelm, K.; Mader, W. Synthesis and Structural Analysis of ϵ -Fe₂O₃. *Z. Anorg. Allg. Chem.* **2005**, *631*, 2383–2389. [[CrossRef](#)]
132. Svendsen, M.B. Beta-Fe₂O₃-Eine Neue Eisen(III)Oxyd-Struktur. *Die Nat.* **1958**, *45*, 542. [[CrossRef](#)]
133. Dachs, V.H. Die Kristallstruktur Des Bixbyits (Fe,Mn)₂O₃. *Z. Krist.* **1956**, *107*, 370–395. [[CrossRef](#)]
134. Sakurai, S.; Namai, A.; Hashimoto, K.; Ohkoshi, S.-I. First Observation of Phase Transformation of All Four Fe₂O₃ Phases (Gamma \rightarrow Epsilon \rightarrow Beta \rightarrow Alpha-Phase). *J. Am. Chem. Soc.* **2009**, *131*, 18299–18303. [[CrossRef](#)] [[PubMed](#)]
135. Linnera, J.; Karttunen, A.J. Lattice Dynamical Properties of Antiferromagnetic MnO, CoO, and NiO, and the Lattice Thermal Conductivity of NiO. *Phys. Rev. B* **2019**, *100*, 144307. [[CrossRef](#)]
136. Risbud, A.S.; Snedeker, L.P.; Elcombe, M.M.; Cheetham, A.K.; Seshadri, R. Wurtzite CoO. *Chem. Mater.* **2005**, *17*, 834–838. [[CrossRef](#)]
137. Will, G.; Masciocchi, N.; Parrish, W.; Hart, M. Refinement of Simple Crystal Structures from Synchrotron Radiation Powder Diffraction Data. *J. Appl. Crystallogr.* **1987**, *20*, 394–401. [[CrossRef](#)]
138. Jiang, Z.; Rappe, A.M. Mechanistic Study of the Li–Air Battery with a Co₃O₄ Cathode and Dimethyl Sulfoxide Electrolyte. *J. Phys. Chem. C* **2021**, *125*, 21873–21881. [[CrossRef](#)]
139. Zasada, F.; Piskorz, W.; Sojka, Z. Cobalt Spinel at Various Redox Conditions: DFT+*U* Investigations into the Structure and Surface Thermodynamics of the (100) Facet. *J. Phys. Chem. C* **2015**, *119*, 19180–19191. [[CrossRef](#)]
140. Kittel, C. *Introduction to Solid State Physics*, 6th ed.; John Wiley & Sons: New York, NY, USA, 1986; ISBN 978-0-471-87474-4.
141. Lide, D. *CRC Handbook of Chemistry and Physics*, 79th ed.; CRC: Boca Raton, FL, USA, 2005; ISBN 0-8493-0485-7.
142. Åsbrink, S.; Norrby, L.J. A Refinement of the Crystal Structure of Copper(II) Oxide with a Discussion of Some Exceptional e.s.d.'s. *Acta Crystallogr. Sect. B Struct. Crystallogr. Cryst. Chem.* **1970**, *26*, 8–15. [[CrossRef](#)]
143. Rödl, C.; Sottile, F.; Reining, L. Quasiparticle Excitations in the Photoemission Spectrum of CuO from First Principles: A GW Study. *Phys. Rev. B Condens. Matter Mater. Phys.* **2015**, *91*, 045102. [[CrossRef](#)]
144. O'Keeffe, M.; Bovin, J.-O. The Crystal Structure of Paramelaconite, Cu₄O₃. *Am. Mineral.* **1978**, *63*, 180–185.
145. Heinemann, M.; Eifert, B.; Heiliger, C. Band Structure and Phase Stability of the Copper Oxides Cu₂O, CuO, and Cu₄O₃. *Phys. Rev. B Condens. Matter Mater. Phys.* **2013**, *87*, 3–7. [[CrossRef](#)]
146. Bolzan, A.; Kennedy, B.; Howard, C. Neutron Powder Diffraction Study of Molybdenum and Tungsten Dioxides. *Aust. J. Chem.* **1995**, *48*, 1473. [[CrossRef](#)]
147. Rogers, D.B.; Shannon, R.D.; Sleight, A.W.; Gillson, J.L. Crystal Chemistry of Metal Dioxides with Rutile-Related Structures. *Inorg. Chem.* **1969**, *8*, 841–849. [[CrossRef](#)]
148. Ben-Dor, L.; Shimony, Y. Crystal Structure, Magnetic Susceptibility and Electrical Conductivity of Pure and NiO-Doped MoO₂ and WO₂. *Mat. Res. Bull.* **1974**, *9*, 837–844. [[CrossRef](#)]
149. Rodriguez, E.E.; Poineau, F.; Llobet, A.; Sattelberger, A.P.; Bhattacharjee, J.; Waghmare, V.U.; Hartmann, T.; Cheetham, A.K. Structural Studies of TcO₂ by Neutron Powder Diffraction and First-Principles Calculations. *J. Am. Chem. Soc.* **2007**, *129*, 10244–10248. [[CrossRef](#)] [[PubMed](#)]
150. Boman, C.-E.; Danielsen, J.; Haaland, A.; Jerslev, B.; Schäffer, C.E.; Sunde, E.; Sørensen, N.A. Refinement of the Crystal Structure of Ruthenium Dioxide. *Acta Chem. Scand.* **1970**, *24*, 116–122. [[CrossRef](#)]
151. Ryden, W.D.; Lawson, A.W. Magnetic Susceptibility of IrO₂ and RuO₂. *J. Chem. Phys.* **1970**, *52*, 6058–6061. [[CrossRef](#)]
152. Shannon, R.D. Synthesis and Properties of Two New Members of the Rutile Family RhO₂ and PtO₂. *Solid State Commun.* **1968**, *6*, 139–143. [[CrossRef](#)]
153. Shirako, Y.; Wang, X.; Tsujimoto, Y.; Tanaka, K.; Guo, Y.; Matsushita, Y.; Nemoto, Y.; Katsuya, Y.; Shi, Y.; Mori, D.; et al. Synthesis, Crystal Structure, and Electronic Properties of High-Pressure PdF₂-Type Oxides MO₂ (M = Ru, Rh, Os, Ir, Pt). *Inorg. Chem.* **2014**, *53*, 11616–11625. [[CrossRef](#)]
154. Richards, R. *Surface and Nanomolecular Catalysis*, 1st ed.; CRC Press: Boca Raton, FL, USA, 2006; ISBN 978-0-367-39081-5.
155. Standke, B.; Jansen, M. Darstellung Und Kristallstruktur von Ag₃O₄. *J. Solid State Chem.* **1987**, *67*, 278–284. [[CrossRef](#)]
156. Tudela, D. Silver(II) Oxide or Silver(I,III) Oxide? *J. Chem. Educ.* **2008**, *85*, 863. [[CrossRef](#)]
157. Standke, B.; Jansen, M. Ag₃O₄, the First Silver(II,III) Oxide. *Angew. Chem. Int. Ed. Engl.* **1986**, *25*, 77–78. [[CrossRef](#)]
158. Palmer, D.; Dickens, P. Tungsten Dioxide: Structure Refinement by Powder Neutron Diffraction. *Acta Cryst.* **1979**, *B35*, 2199–2201. [[CrossRef](#)]
159. Goodenough, J.B.; Pierre, G.; Jean, B. Magnetic and Electric Properties of ReO₂: Theoretical Investigation. *Compt. Rend.* **1965**, *261*, 2331–2335.
160. Gibart, P. Physico-Chemical Properties of Rhenium Dioxides. *Bull. Soc. Chim. Fr.* **1967**, *2*, 444.
161. Wang, S.; Liu, Y.; Yu, Z.; Sheng, X.; Yang, S.A. Hourglass Dirac Chain Metal in Rhenium Dioxide. *Nat. Commun.* **2017**, *8*, 1844. [[CrossRef](#)]
162. Corrêa, H.P.S.; Cavalcante, I.P.; Martinez, L.G.; Orlando, C.G.P.; Orlando, M.T.D. Refinement of Monoclinic ReO₂ Structure from XRD by Rietveld Method Rietveld. *Braz. J. Phys.* **2004**, *34*, 1208–1210. [[CrossRef](#)]

163. Magnéli, A.; Siitonen, S.; Skrifvars, B.; Schliack, J.; Reio, L. Studies on Rhenium Oxides. *Acta Chem. Scand.* **1957**, *11*, 28–33. [[CrossRef](#)]
164. Tribalat, S.; Jungfleisch, J.; Delafosse, D. Sur Les Structures Cristallines Du Dioxyde de Rhenium. *C. R. Acad. Sc. Paris* **1964**, *259*, 2109–2112.
165. Ivanovskii, A.L.; Chupakhina, T.I.; Zubkov, V.G.; Tyutyunnik, A.P.; Krasilnikov, V.N.; Bazuev, V.G.; Okatov, V.S.; Lichtenstein, A.I. Structure and Electronic Properties of New Rutile-like Rhenium (IV) Dioxide ReO_2 . *Phys. Lett. Sect. A Gen. At. Solid State Phys.* **2005**, *348*, 66–70. [[CrossRef](#)]
166. Bolzan, A.A.; Fong, C.; Kennedy, B.J.; Howard, C.J. Structural Studies of Rutile-Type Metal Dioxides. *Acta Crystallogr. Sect. B Struct. Sci.* **1997**, *53*, 373–380. [[CrossRef](#)]
167. Ping, Y.; Galli, G.; Goddard, W.A. Electronic Structure of IrO_2 : The Role of the Metal d Orbitals. *J. Phys. Chem. C* **2015**, *119*, 11570–11577. [[CrossRef](#)]
168. Steinmann, S.N.; Corminboeuf, C. Comprehensive Benchmarking of a Density-Dependent Dispersion Correction. *J. Chem. Theory Comput.* **2011**, *7*, 3567–3577. [[CrossRef](#)] [[PubMed](#)]
169. Tkatchenko, A. Current Understanding of Van Der Waals Effects in Realistic Materials. *Adv. Funct. Mater.* **2015**, *25*, 2054–2061. [[CrossRef](#)]
170. Stephens, J.S.; Cruickshank, D.W.J. The Crystal Structure of $(\text{CrO}_3)_\infty$. *Acta Crystallogr. Sect. B Struct. Crystallogr. Cryst. Chem.* **1970**, *26*, 222–226. [[CrossRef](#)]
171. Sitepu, H. Texture and Structural Refinement Using Neutron Diffraction Data from Molybdate (MoO_3) and Calcite (CaCO_3) Powders and a Ni-Rich $\text{Ni}_{50.7}\text{Ti}_{49.30}$ Alloy. *Powder Diffr.* **2009**, *24*, 315–326. [[CrossRef](#)]
172. Locherer, K.R.; Swainson, I.P.; Salje, E.K.H. Transition to a New Tetragonal Phase of WO_3 : Crystal Structure and Distortion Parameters. *J. Phys. Condens. Matter* **1999**, *11*, 4143–4156. [[CrossRef](#)]
173. Simon, V.A.; Dronskowski, R.; Krebs, B.; Hettich, B. Die Kristallstruktur von Mn_2O_7 . *Angew. Chem.* **1987**, *99*, 160–161. [[CrossRef](#)]
174. Krebs, V.B. Technetium(VIII)-Oxid: Ein Übergangsmetalloxid Mit Molekülstruktur Im Festen Zustand. *Z. Anorg. Allg. Chem.* **1971**, *380*, 146–159. [[CrossRef](#)]
175. Pley, M.; Wickleder, M.S. Two Crystalline Modifications of RuO_4 . *J. Solid State Chem.* **2005**, *178*, 3206–3209. [[CrossRef](#)]
176. Krebs, B.; Hasse, K.D. Refinements of the Crystal Structures of KTcO_4 , KReO_4 and OsO_4 . The Bond Lengths in Tetrahedral Oxoanions and Oxides of d^0 Transition Metals. *Acta Crystallogr.* **1976**, *B32*, 1334–1337. [[CrossRef](#)]
177. Grimme, S.; Ehrlich, S.; Goerigk, L. Effect of the Damping Function in Dispersion Corrected Density Functional Theory. *J. Comput. Chem.* **2011**, *32*, 1456–1465. [[CrossRef](#)] [[PubMed](#)]
178. Pušelj, M.; Ban, Z.; Lukačević, E.; Morvaj, J. On the Preparation of Mercuric Peroxides and Refinement of the α - HgO_2 Structure. *Z. Anorg. Allg. Chem.* **1985**, *528*, 191–194. [[CrossRef](#)]
179. Vannerberg, N.G. Formation and Structure of Mercuric Peroxides. *Arkiv. Kemi.* **1959**, *13*, 515–521.
180. Hesse, W.; Jansen, M.; Schnick, W. Recent Results in Solid State Chemistry of Ionic Ozonides, Hyperoxides, and Peroxides. *Prog. Solid State Chem.* **1989**, *19*, 47–110. [[CrossRef](#)]
181. Puselj, M.; Ban, Z.; Lukačević, E. The Crystal Structure of α -Mercury(II) Peroxide. *J. Appl. Crystallogr.* **1983**, *16*, 357. [[CrossRef](#)]
182. Dovesi, R.; Orlando, R.; Erba, A.; Zicovich-Wilson, C.M.; Civalleri, B.; Casassa, S.; Maschio, L.; Ferrabone, M.; De La Pierre, M.; D’Arco, P.; et al. CRYSTAL14: A Program for the Ab Initio Investigation of Crystalline Solids. *Int. J. Quantum Chem.* **2014**, *114*, 1287–1317. [[CrossRef](#)]
183. Perdew, J.P.; Burke, K.; Ernzerhof, M. Generalized Gradient Approximation Made Simple. *Phys. Rev. Lett.* **1996**, *77*, 3865–3868. [[CrossRef](#)]
184. Adamo, C.; Barone, V. Toward Reliable Density Functional Methods without Adjustable Parameters: The PBE0 Model. *J. Chem. Phys.* **1999**, *110*, 6158–6170. [[CrossRef](#)]
185. Weigend, F.; Ahlrichs, R. Balanced Basis Sets of Split Valence, Triple Zeta Valence and Quadruple Zeta Valence Quality for H to Rn: Design and Assessment of Accuracy. *Phys. Chem. Chem. Phys.* **2005**, *7*, 3297–3305. [[CrossRef](#)]
186. Grimme, S.; Hansen, A.; Brandenburg, J.G.; Bannwarth, C. Dispersion-Corrected Mean-Field Electronic Structure Methods. *Chem. Rev.* **2016**, *116*, 5105–5154. [[CrossRef](#)]
187. Pascale, F.; Zicovich-Wilson, C.M.; López Gejo, F.; Civalleri, B.; Orlando, R.; Dovesi, R. The Calculation of the Vibrational Frequencies of Crystalline Compounds and Its Implementation in the CRYSTAL Code: Crystalline Compounds and the CRYSTAL Code. *J. Comput. Chem.* **2004**, *25*, 888–897. [[CrossRef](#)] [[PubMed](#)]
188. Zicovich-Wilson, C.M.; Pascale, F.; Roetti, C.; Saunders, V.R.; Orlando, R.; Dovesi, R. Calculation of the Vibration Frequencies of α -Quartz: The Effect of Hamiltonian and Basis Set. *J. Comput. Chem.* **2004**, *25*, 1873–1881. [[CrossRef](#)] [[PubMed](#)]
189. Zagorac, D.; Müller, H.; Ruehl, S.; Zagorac, J.; Rehme, S. Recent Developments in the Inorganic Crystal Structure Database: Theoretical Crystal Structure Data and Related Features. *J. Appl. Cryst.* **2019**, *52*, 918–925. [[CrossRef](#)] [[PubMed](#)]
190. Grazulis, S.; Chateigner, D.; Downs, R.T.; Yokochi, A.F.T.; Quiros, M.; Lutterotti, L.; Manakova, E.; Butkus, J.; Moeck, P.; Le Bail, A. Crystallography Open Database—an Open-Access Collection of Crystal Structures. *J. Appl. Crystallogr.* **2009**, *42*, 726–729. [[CrossRef](#)]
191. Grazulis, S.; Daskevicius, A.; Merkys, A.; Chateigner, D.; Lutterotti, L.; Serebryanaya, N.R.; Moeck, P.; Downs, R.T.; Le Bail, A. Crystallography Open Database (COD): An Open-Access Collection of Crystal Structures and Platform for World-Wide Collaboration. *Nucleic Acids Res.* **2012**, *40*, 420–427. [[CrossRef](#)]

192. Momma, K.; Izumi, F. VESTA 3 for Three-Dimensional Visualization of Crystal, Volumetric and Morphology Data. *J. Appl. Cryst.* **2011**, *44*, 1272–1276. [[CrossRef](#)]
193. Freund, H.J.; Pacchioni, G. Oxide Ultra-Thin Films on Metals: New Materials for the Design of Supported Metal Catalysts. *Chem. Soc. Rev.* **2008**, *37*, 2224–2242. [[CrossRef](#)]